

# Hypervelocity flow of dissociating nitrogen downstream of a blunt nose

By M. N. MACROSSAN

Department of Mechanical Engineering, University of Queensland, St. Lucia, Australia

(Received 10 April 1989 and in revised form 8 December 1989)

The nature of the non-equilibrium flow of strongly dissociating nitrogen has been investigated by a series of simulation calculations using non-equilibrium (finite rate) chemical reactions. These were made with the equilibrium flux method (EFM), and the results have been found to compare favourably with experimental results obtained with a free-piston driven shock-tube wind tunnel which was used to obtain interferograms of the flow of pure nitrogen over a blunt-nosed body, 65 mm long at three angles of incidence. No simple relation between the flow with non-equilibrium chemistry and those for frozen or equilibrium chemistry has been found. The problems of relating test flows produced in the shock tunnel to flight conditions are investigated by considering the test flows that might be produced by some 'ideal equivalent wind tunnels'. It is shown that the degree of frozen dissociation in the test flow in a shock tunnel is not a serious matter, but that the large difference in Mach number between shock tunnel flows and flight conditions may be more important.

## 1. Introduction

In hypervelocity flows the stagnation enthalpy can be large enough to cause dissociation of air in the stagnation region ahead of a blunt body. The effects of this dissociation may extend over a large part of a typical aerodynamic vehicle so that the nature of the flow downstream of the stagnation region is important in the aerodynamic design of such vehicles. This was displayed most dramatically when the Shuttle Orbiter experienced a hypersonic pitching moment significantly different from the pre-flight predictions (Maus, Griffith & Szema 1984). These predictions were obtained from extensive wind-tunnel testing in test facilities which could not produce the 'real gas' effects arising from chemical reactions in the air. The Shuttle flight and design data have been reanalysed using computational methods which incorporate equilibrium chemistry throughout the flow (Griffith *et al.* 1987) but Stalker (1989) has suggested that consideration of equilibrium chemistry alone may be insufficient. In this paper some aspects of hypervelocity flow, with non-equilibrium chemical reactions, are investigated through a series of computations and experiments using pure nitrogen as the test gas. The only chemical reactions in the flow are those for nitrogen dissociation:



where  $k_{f,1}$  and  $k_{f,2}$  are the forward reaction rate constants associated with the collision partners N and N<sub>2</sub> respectively. These reactions, and the similar reactions

for oxygen dissociation, give a good qualitative description of the real-gas behaviour of air and it is useful to study their effects in isolation.

Some preliminary experimental results, obtained in the free-piston driven shock-tube wind tunnel, T3, at the Australian National University were reported previously (Macrossan & Stalker 1987) and Stalker has made available some further results which are presented here for the first time. These results consist of interferograms of the flow, and therefore do not yield a great deal of information which would be useful for the detail design of an aerodynamic vehicle. However, the experimental results are consistent with the results of computations made with a new method for chemically reacting flows, the equilibrium flux method (EFM) (Pullin 1980; Macrossan 1989). Therefore, the calculation method can be used with some confidence to investigate various aspects of the flow of a dissociating gas which cannot be easily investigated using currently available test facilities. Hornung (1976) and Stalker (1989) have used approximate analyses to show the importance of chemical non-equilibrium effects in hypervelocity flows. That work suggests that the design of hypervelocity aerodynamic vehicles will require large-scale computational effort and related experimental investigation if the non-equilibrium nature of reacting gas flow is to be understood properly.

It is the purpose of this work to use the calculation method to demonstrate the chemical non-equilibrium effects in the flow produced by the shock-tube wind tunnel. The phenomenon of reaction 'quenching' (Hornung 1988; Stalker 1989) is discussed, and the effects of chemical non-equilibrium on the aerodynamic forces acting on the model are demonstrated. These results show that consideration of equilibrium chemistry alone is not sufficient to predict the centre of pressure in a non-equilibrium chemically reacting flow.

If shock-tube wind tunnels ('shock tunnels') are to be used to aid the design of hypervelocity aerodynamic vehicles some problems must be addressed. One is the problem of the short test times associated with high-enthalpy operation of a shock tunnel. Another is the problem of the correlation of experimental results with typical flight conditions, given some marked differences between test and flight conditions. In the experiments reported here there exists a degree of frozen dissociation of about 10% in the test-section flow, which is typical of the amount produced by high-enthalpy shock tunnels having nitrogen or air as the test gas. This frozen dissociation arises because the very hot test gas produced by the shock tube, which is subsequently fed into the nozzle, is in an equilibrium state with dissociation levels of about 20–30%. As the test gas passes down the nozzle, recombination takes place too slowly to maintain equilibrium. The dissociation 'freezes' at a value higher than would be achieved for chemical equilibrium throughout the nozzle flow. In contrast, for flight in the atmosphere the free stream is not dissociated and is in chemical equilibrium. Also the static temperature of the test gas is about 4000 K so that when the test and flight velocities are similar the Mach number in the test section is much lower than for flight conditions.

A second purpose of this work is to use the calculation method to address these problems associated with the shock tunnel. It is shown that a fully developed, dissociated flow can be obtained in the short duration of the test flow in the shock tunnel. Also, the effects of free-stream dissociation in the test flow are investigated by comparing the calculated flow in the test section with the flow calculated for two hypothetical wind tunnels which are supposed to provide a hypervelocity flow with the same stagnation enthalpy as the real shock tunnel but with either (i) chemical equilibrium in the free-stream (giving a small change in Mach number), or (ii) no

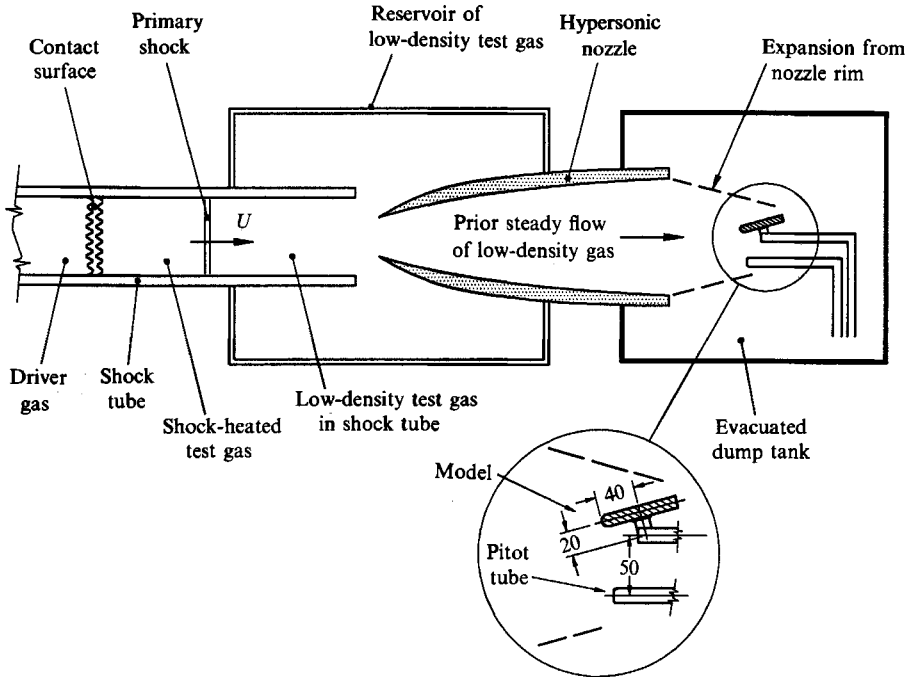


FIGURE 1. Experimental arrangement.

dissociation in the free stream but the same Mach number as in the real shock tunnel. It is concluded that the frozen, non-zero dissociation in the free stream of the test flow is not a serious problem. Finally, the effects of the large difference in Mach number between test and flight conditions are touched upon.

## 2. Experiment

When operated in the normal reflected-shock mode the T3 shock tunnel suffers from severe contamination of the test gas by the driver gas when the stagnation enthalpy is above 25 MJ/kg (Crane & Stalker, 1977). This can be avoided by operating in the non-reflected-shock mode in which the test gas behind the primary shock in the shock tube is fed directly into the nozzle without being reflected. The steady flow obtained in the test section is not maintained for as long as for reflected-shock operation and would be disrupted by fragments of any light diaphragm separating the shock tube and the nozzle. Therefore the prior-steady-flow technique (Mudford & Stalker 1976) was used, in which there is no diaphragm but there is a large reservoir of low-density test gas provided at the end of the shock tube (see figure 1). This reservoir supplies the steady flow of low-density test gas which is set up through the nozzle and into the evacuated dump tank before the high density test gas behind the primary shock in the shock tube reaches the nozzle inlet.

Figure 1 shows the axisymmetric nozzle with its 38 mm diameter intake located at the end of the shock tube, which was 76 mm in diameter. The nozzle expands the shock-heated test gas to a design area ratio of 16, producing hypersonic flow in the test section. In order to reduce the starting time of the nozzle flow, the nozzle was truncated at 300 mm from the intake to yield an exit diameter of 132 mm. The flow produced by this nozzle has been calibrated with air, argon and a mixture of



FIGURE 2. Typical interferogram taken at  $15\ \mu\text{s}$  after the test gas impinged on the leading edge. Nominal test-section conditions:  $u_\infty = 6.36 \times 10^3\ \text{m/s}$ ,  $\rho_\infty = 4.41 \times 10^{-2}\ \text{kg/m}^3$ ,  $T_\infty = 4415\ \text{K}$ ,  $\alpha_\infty = 0.094$ ,  $M_\infty = 4.55$ . Angle of incidence =  $15^\circ$ ,  $r_n = 5\ \text{mm}$ .

hydrogen and neon as test gases (Mudford & Stalker 1976, 1980), and it has been found that in each case the flow is uniform and parallel to within  $\pm 2^\circ$ . A Pitot probe, consisting of a bar gauge, with a PZT piezoelectric sensing element, in a bar of 3 mm diameter, was mounted in a 12 mm diameter housing, with its axis 50 mm below the tunnel centreline, and its upstream face 82 mm downstream of the nozzle exit. The test model was a flat plate, 65 mm long, 100 mm wide, and 10 mm thick, with a cylindrical nose of radius 5 mm. It was attached to a string by a swivel mount, so that its incidence could be varied. The entire width of the model and the upstream face of the Pitot probe were accommodated within the uniform region of the test flow.

Mach Zehnder interferograms of the flow over this model were obtained using a Carl Zeiss interferometer, with illumination provided by a 5 ns pulse from a rhodium-G dye laser, operating at a wavelength of 590 nm. A typical interferogram, taken at  $15\ \mu\text{s}$  after the test gas impinged on the leading edge of the model, is shown in figure 2. No side plates were provided on the model to ensure two-dimensional flow and it was estimated (Macrossan & Stalker 1987) that, at about 10 mm from the trailing edge of the plate, edge effects would introduce a shift of  $-0.15$  fringes at the surface of the plate, and  $+0.3$  fringes at the shock wave, with a positive fringe shift indicating a density increase. These are small enough for edge effects to be neglected as a first approximation.

### 3. Chemical model for nitrogen

For the sake of simplicity, it is assumed throughout this work that nitrogen may be adequately represented by Lighthill's ideal dissociating gas (IDG) model (Lighthill 1957). The law of mass action for this IDG model may be written as

$$\frac{\alpha^2}{1-\alpha} = \frac{\rho_d}{\rho} \exp\left(\frac{-\theta_d}{T}\right), \quad (2)$$

where  $\rho$  is density,  $T$  is temperature,  $\alpha = [\text{N}]/([\text{N}] + 2[\text{N}_2])$  is the mass fraction of dissociated nitrogen,  $\theta_d = 113200$  K is the characteristic dissociation temperature and  $\rho_d$  (the characteristic density) represents a combination of terms in the partition functions for N and N<sub>2</sub> which is taken by Lighthill to be constant. It turns out that the assumption that  $\rho_d$  is constant is equivalent to representing the sum of the equilibrium values of energy of electronic and vibrational excitation by the energy of a single degree of freedom for the diatomic species which is fully excited at all temperatures. For N<sub>2</sub>, a value of  $\rho_d = 130$  gm/cm<sup>3</sup> is recommended by Lighthill. From (2) the equilibrium constant for the IDG model, based on molar concentrations, is

$$K_c = \frac{4\rho_d}{W} \exp\left(\frac{-\theta_d}{T}\right), \quad (3)$$

where  $W$  is the molar mass of N<sub>2</sub>. The equation of state for a mixture of molecular and atomic nitrogen is

$$p = \rho(1 + \alpha) R_{nn} T, \quad (4)$$

where  $p$  is pressure and  $R_{nn}$  is the ordinary gas constant for N<sub>2</sub>. The specific enthalpy for the IDG model is given by

$$h = R_{nn}[\alpha\theta_d + (4 + \alpha) T]. \quad (5)$$

The rate equation giving the combined rate of production of dissociated nitrogen for the reactions in (1) may be written in terms of the degree of dissociation, and is (Vincenti & Kruger 1965, p. 232)

$$\frac{d\alpha}{dt} = \frac{\rho}{W} [2\alpha k_{r,1} + (1-\alpha) k_{r,2}] \left[ (1-\alpha) - \frac{4\rho\alpha^2}{WK_c} \right]. \quad (6)$$

Freeman (1958) put this equation in a form appropriate for the IDG model by substituting from (3) for  $K_c$ . Thus, with the rate constants in the usual form

$$k_{r,i} = C_i T^{\eta_i} \exp(-\theta_d/T), \quad (7)$$

where  $C_i$  and  $\eta_i$  are constants, (6) becomes

$$\frac{d\alpha}{dt} = \rho X(\alpha, T) \left[ (1-\alpha) \exp\left(\frac{-\theta_d}{T}\right) - \frac{\rho\alpha^2}{\rho_d} \right], \quad (8)$$

with

$$X(\alpha, T) = \frac{2C_1 T^{\eta_1} \alpha + C_2 T^{\eta_2} (1-\alpha)}{W}. \quad (9)$$

	Reference	$C_1^{(1)}$	$\eta_1$	$C_2^{(1)}$	$\eta_2$	$C^{(2)}$	$\eta$
I.	Appleton <i>et al.</i> (1968)	$1.6 \times 10^{22}$	-1.6	$3.7 \times 10^{21}$	-1.6	$5.0 \times 10^{22}$	-1.6
II.	Kewley & Hornung (1974)	$8.5 \times 10^{25}$	-2.5	$2.3 \times 10^{20}$	-3.5	$2.7 \times 10^{24}$	-2.5
III.	Byron, Cary (1966, 1965)	$3.0 \times 10^{22}$	-1.5	$4.8 \times 10^{21}$	-1.5	$9.0 \times 10^{20}$	-1.5
IV.	Hanson & Baganoff (1972)	$2.2 \times 10^{26}$	-2.5	$3.9 \times 10^{23}$	-4.5	$6.9 \times 10^{24}$	-2.5

*Notes:*

(1) The combination  $C_1 T^{\eta_1}$  or  $C_2 T^{\eta_2}$ , where  $T$  is in degrees Kelvin, has the dimensions of  $\text{cm}^3 \text{mole}^{-1} \text{s}^{-1}$ .

(2) The combination  $CT^\eta$ , where  $T$  is in degrees Kelvin, has the dimensions of  $\text{cm}^3 \text{g}^{-1} \text{s}^{-1}$ .

TABLE 1. Reaction-rate parameters for nitrogen dissociation

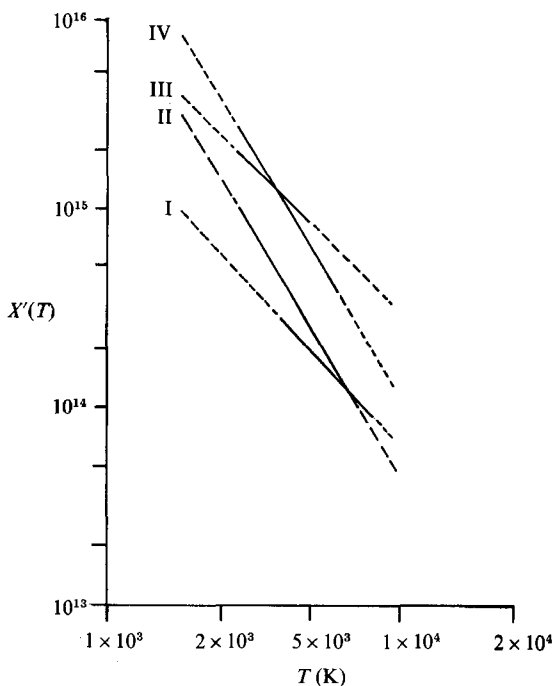


FIGURE 3. Experimentally determined reaction rates compared using the function  $X'(T)$  of (11) with  $C$  and  $\eta$  from table 1: —, range of experimental measurement; ---, extrapolation; I, Appleton *et al.* (1968); II, Kewley & Hornung (1974); III, Byron (1966) and Cary (1965); IV, Hanson & Baganoff (1972).

Freeman made the further simplifying assumption that  $X(\alpha, T)$  could be replaced by a function of  $T$  only so that the reaction rate would be

$$\frac{d\alpha}{dt} = \rho X'(T) \left[ (1 - \alpha) \exp\left(\frac{-\theta_d}{T}\right) - \frac{\rho \alpha^2}{\rho_d} \right] \quad (10)$$

$$\text{with} \quad X'(T) = CT^\eta, \quad (11)$$

where  $C$  and  $\eta$  are constants to be determined. In some of the calculations reported

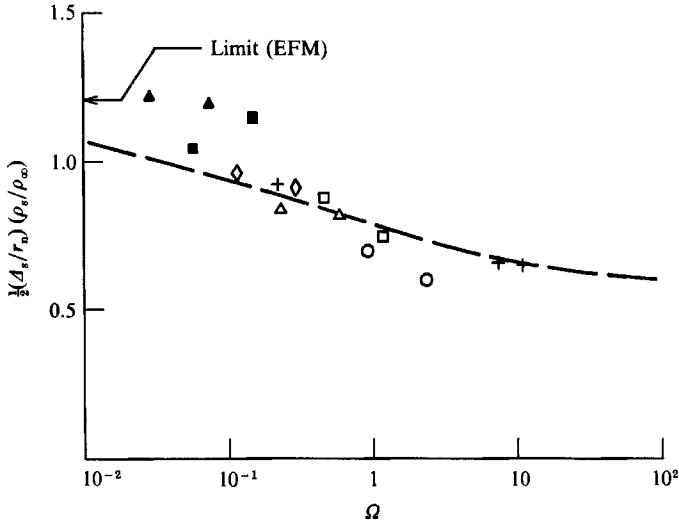


FIGURE 4. Shock stand-off distances in reacting flow: Hornung's (1972) figure 21 reconsidered. Experiments: low-enthalpy data with  $r_n$ :  $\blacktriangle$ ,  $\frac{1}{16}$  in.;  $\blacksquare$ ,  $\frac{1}{8}$  in.;  $\blacklozenge$ ,  $\frac{1}{4}$  in.;  $\blacktriangle$ ,  $\frac{1}{2}$  in.;  $\square$ , 1 in.;  $\circ$ , 2 in.  $\Omega$  calculated using  $C_1 = 8.5 \times 10^{25}$ ,  $\eta_1 = -2.5$ ,  $C_2 = 2.3 \times 10^{26}$ ,  $\eta_2 = -3.5$ . Calculations: ———, Hornung's (1972); +, EFM.

here the reaction rate in (8) and (9) has been used, and in others, the reaction rate of (10) and (11).

Values of the exponent  $\eta_i$  in (7) determined by experiment (Cary 1965; Byron 1966; Appleton, Steinberg & Liquornik 1968; Hanson & Baganoff 1972; Kewley & Hornung 1974) vary from  $-4.5$  to  $-1.5$  and the values of  $C_i$  found in these experiments also vary greatly. Four sets of constants ( $C_1$ ,  $\eta_1$ ,  $C_2$ ,  $\eta_2$ ) are given in table 1, where the results of Cary (1965) and Byron (1966) have been combined into a compromise set as suggested by Byron (1966). Also shown for each set are values of  $C$  and  $\eta$  which make the functions  $X(\alpha, T)$  and  $X'(T)$ , and hence the reaction rates of (8) and (10), reasonably close over the range of conditions in the experiments. Figure 3 shows the different experimentally determined reaction rates compared on the basis of the equivalent functions  $X'(T)$  and it can be seen that there are great differences in the reaction rates in the range of temperatures 5000–10000 K behind the oblique shock in the present flow (see figure 26). Some indirect experimental results for nitrogen reaction rates are the shock stand-off distances for nitrogen measured by Hornung (1972), who compared his data with calculations of shock stand-off distance on the basis of the reaction rate parameter

$$\Omega = \left( \frac{d\alpha}{dt} \right)_f \left( \frac{r_n}{u_\infty} \right), \quad (12)$$

where  $r_n$  is the model nose radius (5 mm),  $u_\infty$  is the fluid velocity in the test section and  $(d\alpha/dt)_f$  is the reaction rate of (8) evaluated for conditions calculated immediately behind the normal shock with the chemical composition frozen across the shock. Hornung used Cary's (1965) reaction rate and found that experiment and calculations did not agree. However, if Hornung's data for the two low-enthalpy runs alone – these being the only ones for which T3 is now known to provide an uncontaminated test gas (Crane & Stalker 1977) – are reconsidered on the basis of reaction rate set II in table 1 the agreement between calculation and experiment is much better. This is

shown in figure 4, which together with the fact that set II of the reaction-rate data agrees, within the experimental error, with at least one of the other sets over the entire temperature range (Kewley & Hornung 1974) suggests that reaction rate set II can be used with reasonable confidence. It is also reassuring that for the temperatures of interest here (5000–10000 K) set II agrees most closely with the results of Appleton *et al.* (1968) which had previously been considered the most reliable by Baulch *et al.* (1973).

#### 4. Test-section conditions

The shock speed in each run was determined to within 2% from the measurement of the shock transit time between a number of pressure transducers fitted along the length of the shock tube. The shock decelerates as it travels the length of the tube and, since each portion of shock-heated test gas which enters the nozzle was processed by a shock of different strength, the nozzle flow is unsteady. The nominal 'steady' conditions in the test section were determined by first using the average speed of the shock over the second half of the shock tube and the known initial test-gas filling pressure to determine the average conditions in the gas behind the primary shock. Then the steady non-equilibrium flow of this 'average gas' was calculated for a quasi-one-dimensional nozzle expansion, with a linear variation of area ratio up to 16 at a distance of 300 mm, this variation being chosen to represent the expansion along a typical streamline in the nozzle.

Tables 2(a) and 2(b) show the conditions behind the primary shock (the nozzle inlet conditions) for the only two runs for which the magnitude of the Pitot pressure in the test section was recorded. Also shown are the nozzle exit conditions (the test-section conditions) and the corresponding Pitot pressure, calculated with different choices of the experimentally determined values of ( $C_1, \eta_1, C_2, \eta_2$ ) in conjunction with (8) and (9). The Pitot pressure in the test section is almost independent of the assumed reaction rate and in each case agrees with the measured value to within the estimated experimental error.

The differences between the nominal post-shock properties shown in the tables and those calculated using a chemical model for nitrogen (Marrone 1962) which does not use the simplifying assumption of (3) were found to be 3.3% for density, 0.3% for velocity, 1.3% for temperature, 0.4% for pressure and 12% for the degree of dissociation. Tables 2(a) and 2(b) show the differences in the nozzle inlet conditions obtained by varying the shock speed by 2% from its nominal value. Since the two sets of differences are comparable there seems to be little point in using a chemical model more rigorous than the IDG model, a view which is supported by the good agreement between the shock stand-off distances calculated using EFM with the IDG model (these are shown in figure 4 and are discussed later) and those calculated by Hornung (1972) using Marrone's (1962) chemical model.

Tables 2(a) and 2(b) also show that the set of test-section conditions obtained with Kewley & Hornung's (1974) reaction-rate data are in the middle of the range of conditions predicted with the other reaction rates. In subsequent work the test-section conditions have been calculated using this set of reaction-rate constants which, as mentioned before, appears to be the best available.

In these experiments  $\Omega$ , equation (12), ranged from 8.6 to 12.4, values which are a little larger than the value of  $\Omega \approx 1$  for which the effect of non-equilibrium chemistry might be most marked. However, Hornung's (1972) calculations of dissociating nitrogen flow over spheres and cylinders suggest that the limit of

(a)		Nozzle exit (test section) conditions nozzle design area ratio = 16				
		Pre-shock	Nozzle inlet	Rate <sup>(1)</sup> I	Rate II	Rate III
Run 61						
Density (10 <sup>-2</sup> kg/m <sup>3</sup> )	8.31	91.2 (2%)	4.59	4.58	4.57	4.57
Velocity <sup>(2)</sup> (10 <sup>3</sup> m/s)	5.80 (2%)	5.27 (2%)	6.56	6.57	6.58	6.58
Temperature (K)	293	7723 (1%)	3993	4668	4673	5130
Mach number	17.03	2.66 (2%)	4.81	4.53	4.54	4.37
Static pressure (atm)	0.0723	25.5 (4%)	0.617	0.702	0.701	0.759
Dissociation	0.0	0.219 (7%)	0.135	0.108	0.107	0.091
Pitot <sup>(3)</sup> pressure (atm)	—	—	19.3	19.5	19.5	19.6

*Notes:*

- (1) Nozzle exit conditions have been calculated with the four different sets of reaction parameters given in Table 1.
- (2) Pre-shock fluid velocity is relative to the shock. All other velocities are relative to the laboratory.
- (3) Measured Pitot pressure was 19.0 atm at  $t = 42 \mu\text{s}$ .
- (4) Numbers in brackets are the % change in a derived quantity for a 2% change in shock speed.

(b)		Nozzle exit (test section) conditions nozzle design area ratio = 16				
		Pre-shock	Nozzle inlet	Rate <sup>(1)</sup> I	Rate II	Rate III
Run 60						
Density (10 <sup>-2</sup> kg/m <sup>3</sup> )	6.07	70.6 (2%)	3.59	3.59	3.58	3.58
Velocity <sup>(2)</sup> (10 <sup>3</sup> m/s)	6.12 (2%)	5.59 (2%)	6.87	6.89	6.90	6.90
Temperature (K)	293	7836 (1%)	4032	4746	4823	5259
Mach number	17.97	2.73 (2%)	4.90	4.61	4.59	4.43
Static pressure (atm)	0.0528	20.84 (4%)	0.506	0.580	0.586	0.631
Dissociation	0.0	0.268 (7%)	0.177	0.149	0.144	0.130
Pitot <sup>(3)</sup> pressure (atm)	—	—	16.7	16.8	16.8	16.8

*Notes:*

- (1) Reaction rate parameters are given in Table 1.
- (2) Pre-shock fluid velocity is relative to the shock. All other velocities are relative to the laboratory.
- (3) Measured Pitot pressure was 16.7 atm at  $t = 40 \mu\text{s}$ .
- (4) Numbers in brackets are the % change in a derived quantity for a 2% change in shock speed.

TABLE 2. Flow conditions for two typical runs

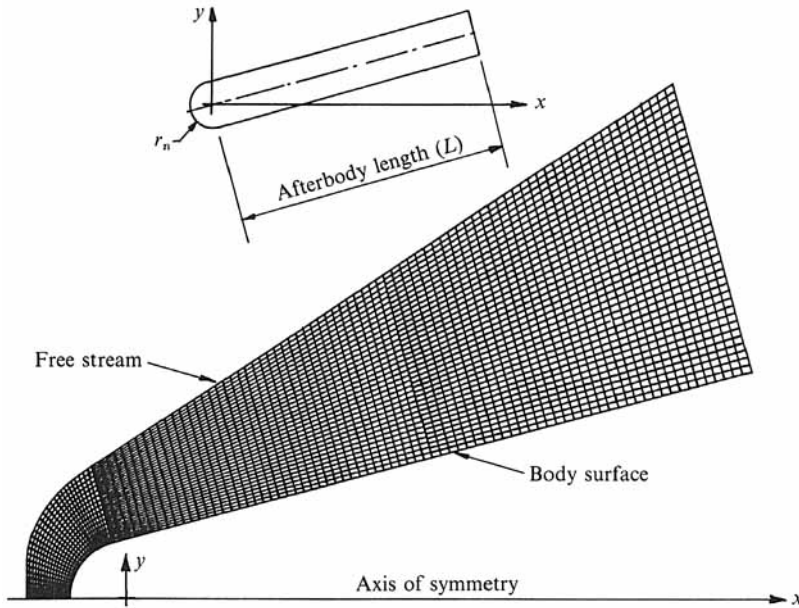


FIGURE 5. Computational grid for the blunt flat plate at an incidence of  $15^\circ$ . The grid contains 3268 cells.

chemical equilibrium flow is not achieved for values of  $\Omega$  less than 100, so some non-equilibrium effects would be expected to appear.

## 5. Calculation method and validation

Calculations for an impulsively started unsteady flow, with free-stream conditions matching the nominal test-section conditions in the experiments, were made using a new finite-volume technique, the equilibrium flux method (EFM), developed by Pullin (1980) as the high-density (or infinite collision rate) limit of Bird's Direct Simulation Method (Bird 1976). The method was adapted for chemically reacting flows by Macrossan (1989). The computational flow field is divided into a large number of small cells, as shown in figure 5, and the unsteady development of the flow is followed by allowing the cells to exchange mass, momentum and energy in a series of small time steps. The fluxes (/unit time) of mass, momentum and energy across an element  $\hat{n} dA$  of an interface between two cells, where  $\hat{n}$  is the surface normal, are obtained from the expression derived from kinetic theory:

$$\int_{-\infty}^{\infty} Q n f(\mathbf{c}) \cdot \hat{n} dA d\mathbf{c},$$

where  $Q$  represents the mass, momentum or energy of a single molecule,  $n$  is the molecular number density and  $f(\mathbf{c})$  is the distribution function for molecular velocity  $\mathbf{c}$ . To ensure that information is transmitted in the physically correct directions in EFM,  $f(\mathbf{c})$  on the interface between two cells is composed of two truncated Maxwellian distributions, one for  $\mathbf{c} \cdot \hat{n} > 0$ , which corresponds to the conditions in the cell on one side of the interface, and another for  $\mathbf{c} \cdot \hat{n} < 0$ , which corresponds to conditions on the other side. Along the upstream edge of the flow field the boundary conditions are constant and set equal to the nominal free-stream conditions. At the

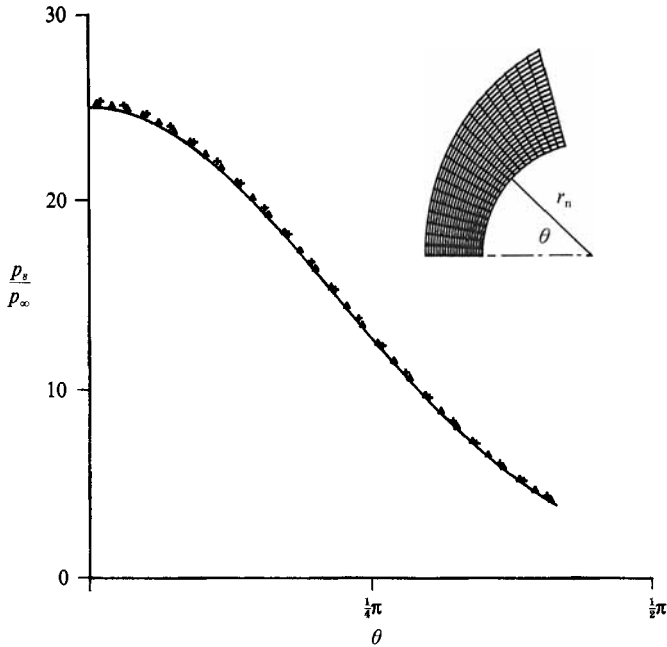


FIGURE 6. Surface pressure on blunt nose for EFM calculations with different grids: +,  $20 \times 20$ ; ▲,  $30 \times 30$ ; —,  $100 \times 100$ . Free-stream conditions:  $u_\infty = 5.5 \times 10^3$  m/s,  $\rho_\infty = 2.0 \times 10^{-2}$  kg/m<sup>3</sup>,  $T_\infty = 4000$  K,  $\alpha_\infty = 0.0018$ ,  $M_\infty = 4.37$  and  $r_n = 5$  mm. Reaction-rate parameters (c.g.s. units):  $C = 2.7 \times 10^{24}$ ,  $\eta = -2.5$ .

axis of symmetry and along the body surface molecular fluxes are, in effect, reflected specularly which gives the usual velocity slip condition for the Euler equations. At the downstream boundary the fluxes are calculated assuming that there are no gradients of any flow properties normal to the boundary. The calculations began with uniform free-stream conditions throughout the flow field and were continued until steady conditions were reached. Non-equilibrium chemical reactions are accounted for by a simple decoupling of the convection and chemical reaction processes.

A complete description of the method is given elsewhere (Macrossan 1989) where it is shown that the method provides an approximate solution of the Euler equations with added pseudo-dissipative terms. The pseudo-dissipation is related to the cell size and hence the results can never be entirely independent of the computational grid; for example the shocks are smeared over a few cell widths. Convergence to the correct solution for a chemically reacting flow behind a one-dimensional normal shock has been demonstrated before (Macrossan 1989) but because of limits on the computational power then available the demonstration of convergence for two-dimensional flows was perhaps not quite so convincing, but will be supplemented here.

The reaction rate behind the bow shock is much greater than elsewhere in the flow and the convergence of the calculation method for decreasing cell sizes in the stagnation region is a severe test of the method. Consider the surface pressure distributions around the blunt nose shown in figure 6 which were obtained for different computational grids confined to the nose region. Between the coarsest ( $20 \times 20$ ) and the finest ( $100 \times 100$ ) grid the change in pressure is less than 1% near the stagnation point and about 4% near the downstream boundary, where some small error might be expected to arise from the downstream boundary condition

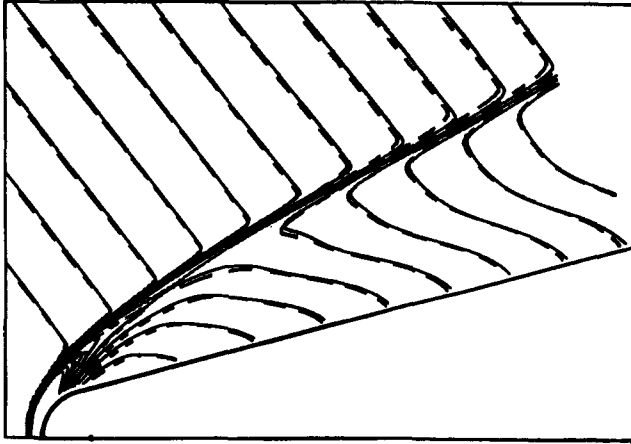


FIGURE 7. Fringe patterns at  $t = 60 \mu\text{s}$  after impulsive start of flow, obtained with different grids. —, 7670 cells. ---, 3268 cells with small offset in fringe number. Free-stream conditions:  $u_\infty = 6.09 \times 10^3 \text{ m/s}$ ,  $\rho_\infty = 5.75 \times 10^{-2} \text{ kg/m}^3$ ,  $T_\infty = 4606 \text{ K}$ ,  $\alpha_\infty = 0.081$ ,  $M_\infty = 4.3$  and  $r_n = 5 \text{ mm}$ . Reaction-rate parameters (c.g.s. units):  $C = 2.78 \times 10^{20}$ ,  $\eta = -1.5$ .

described above. The shock stand-off distance,  $\Delta_s$ , determined from the point where the sonic line crosses the stagnation streamline, was found for different grids. It decreased linearly with the size,  $\Delta x$ , of the cells along the stagnation line to a limiting value of  $\Delta_s/r_n = 0.247$ . For the same free-stream conditions, but with the reactions frozen, the value of  $\Delta_s/r_n$  was found to be 0.456. These values are shown in figure 4, along with other values of  $\Delta_s$  found previously using EFM (Macrossan 1989), and agree well with the calculations and experimental results of Hornung (1972). For a cell size  $\Delta x/r_n = 0.005$ ,  $\Delta_s$  was 2.4% greater than the limiting value and for  $\Delta x/r_n = 0.0125$  was 6% greater. The latter value of  $\Delta x$  was the size of the cells along the stagnation line in the larger grids (see figure 5) which were used to obtain most of the following results.

The complete flow also was calculated for different computational grids, each similar to that shown in figure 5 and the total force acting on the afterbody at a time of  $60 \mu\text{s}$  after the impulsive start of the flow was resolved into force coefficients  $C_x$  and  $C_y$ . These were normalized with respect to the free-stream density  $\rho_\infty$ , velocity  $u_\infty$ , and the afterbody length of the model, denoted  $L$  (see figure 5). Thus

$$C_x = 2 \sum_s p_s \Delta s \sin \theta_s / (\rho_\infty u_\infty^2 L) \quad (13)$$

and

$$C_y = 2 \sum_s p_s \Delta s \cos \theta_s / (\rho_\infty u_\infty^2 L) \quad (14)$$

where  $p_s$  is the surface pressure,  $\Delta s$  is the corresponding surface segment length and  $\theta_s$  is the angle the surface makes with the  $x$ -axis. The pressure forces contributing to  $C_x$  and  $C_y$  are those acting on the windward side of the model only. The value of  $C_x$  calculated on the coarsest grid (1100 cells) differed by 10% from that calculated on the finest grid (7670 cells) and the corresponding change in  $C_y$  was 3%. For the grid in figure 5 (3268 cells),  $C_x$  and  $C_y$  differed by 0.3% and 0.1% respectively from the corresponding values for the finest grid. The position of the centre of pressure changed by less than 0.5% of  $L$  between the finest and the coarsest grids.

These results suggest that the grid in figure 5 provides adequate resolution and this

conclusion can be tested further by comparing the entire flow fields calculated with different computational grids. A convenient way to do this is to construct an interferogram fringe pattern for the computed flow. The fringe shift  $F$  at any point is given by

$$F = 0.24\Delta\rho(1 + 0.28\alpha)(P/\lambda), \quad (15)$$

where  $\lambda$  is the wavelength,  $P$  is the optical path length and  $\Delta\rho$  is the density rise in  $\text{kg/m}^3$  (Hornung 1972). An optical path length of 100 mm and a wavelength of 590 nm, which were the values for the experimental set-up, were used. Figure 7 shows the fringe patterns for 3268 and 7670 cells, with a small offset in fringe number to differentiate between them. It is clear that the grid with fewer cells is adequate.

The fineness of the computational grid can be measured by a reaction-rate parameter  $\omega$ , similar to that in (12), given by

$$\omega = \frac{\Delta \, d\alpha}{u \, dt}, \quad (16)$$

where  $u$  is the fluid velocity in a cell,  $\Delta$  is an approximate cell dimension measured in the direction of  $u$ , and  $d\alpha/dt$  is the reaction rate in the cell. The average value,  $\bar{\omega}$ , over all the cells, except those which contain virtually undisturbed free-stream conditions, is a measure of the overall computational fineness of the grid. The grid with 3268 cells had a value of  $\bar{\omega} = 1.8 \times 10^{-3}$  and grids for which the value of  $\bar{\omega}$  was of about the same magnitude or slightly smaller than this were used in all the remaining calculations reported here.

## 6. Flow starting time

In view of the short period of reasonably steady flow which can be obtained from the shock tunnel it is important to find the time required to reach a steady flow over the model. It was found previously (Macrossan & Stalker 1987), from a series of interferograms of the flow at various stages of development, that the flow was fully developed within about 20–30  $\mu\text{s}$  from the time the test gas first impinged on the leading edge of the model. The EFM calculations can be used to get another estimate of the time for a steady flow to be developed.

Figure 8 shows the development of the density field calculated at various times after the impulsive start of the flow, for the same nominal free-stream conditions as in the experiments. The density field at  $t = 35 \mu\text{s}$  is virtually indistinguishable from that at  $t = 60 \mu\text{s}$ , which is shown in figure 27(a).

The force coefficients  $C_x$  and  $C_y$  have been determined from the computations for the developing flow shown in figure 8 as well as the moment coefficient given by

$$C_m = (C_x Y_{cp} - C_y X_{cp})/L, \quad (17)$$

where  $(X_{cp}, Y_{cp})$  are the co-ordinates of the centre of pressure relative to the coordinate system shown in figure 5. All three coefficients were within 3% of their steady-state values at  $t = 25 \mu\text{s}$ , which is close to the starting time determined from the interferograms, despite the slightly different starting conditions in the two cases. By  $t = 35 \mu\text{s}$  all three coefficients were within 0.4% of the steady-state values. This time corresponds to the free-stream flow traversing 3.5 body lengths. To ensure that a steady state has been reached in all subsequent calculations, the computations have been continued until the free stream had traversed at least 4 body lengths

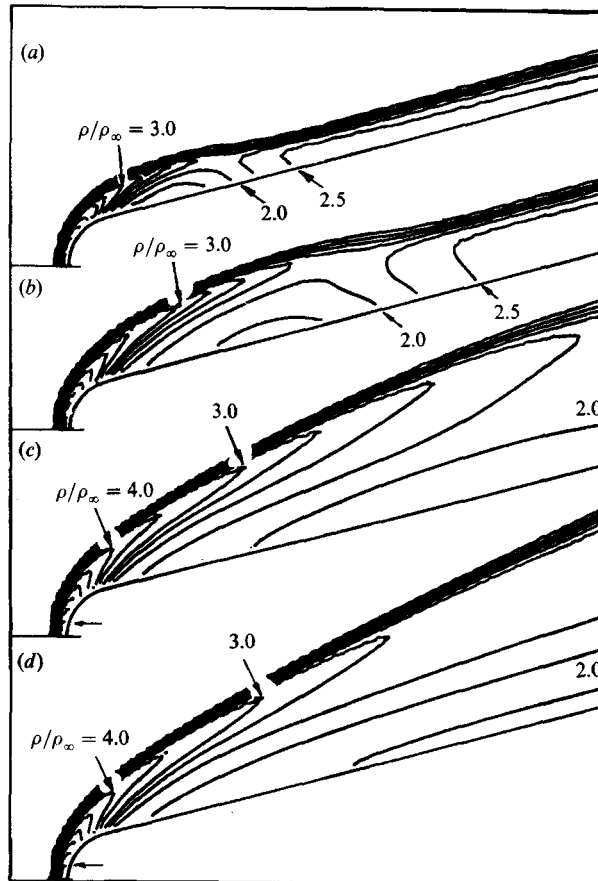


FIGURE 8. Calculated unsteady development of the flow shown by density contours at various instants after the impulsive start of the flow. (a)  $t = 2.8 \mu\text{s}$ , (b)  $6 \mu\text{s}$ , (c)  $15 \mu\text{s}$ , (d)  $35 \mu\text{s}$ . Free-stream conditions as for figure 2. Reaction-rate parameters (c.g.s. units):  $C_1 = 8.5 \times 10^{25}$ ,  $\eta_1 = -2.5$ ,  $C_2 = 2.3 \times 10^{29}$ ,  $\eta_2 = -3.5$ .  $\Omega = 9.9$ .

## 7. Simulation and experimental results compared

Table 3 shows the nominal test-section conditions, calculated as explained in §4, for the runs in which interferograms of the fully developed flow were obtained. Simulation calculations using the corresponding free-stream conditions have been made for the body at angles of incidence of  $0^\circ$ ,  $15^\circ$  and  $30^\circ$  and figures 9, 10 and 11 show interferograms and computed fringe patterns derived from the simulation results. The exact position of the shock in both the experiments and the simulations is uncertain: in the experiments because of the shock curvature in the transverse direction and in the simulations because the shock is smeared over a few cell widths. However, the figures show that the simulations give a good indication of the shock location, and also of the position of the maximum fringe shift in the one case ( $30^\circ$  incidence) where this maximum is not right at the shock location.

To compare the experiments and the simulations more closely it is necessary to compare fringe shifts at different locations in the flow. Since the individual fringes on the interferogram cannot be traced through the shock the minimum and maximum fringe shifts which can be expected behind the shock must be calculated by

Run No.	60	55	63
Model incidence	0°	15°	30°
Density ( $10^{-2}$ kg/m <sup>3</sup> )	3.59	4.41	4.31
Velocity ( $10^3$ m/s)	6.89	6.36	6.23
Temperature (K)	4746	4415	4256
Dissociation	0.149	0.094	0.086
Mach number	4.61	4.55	4.56
$\Omega^{(1)}$	12.4	9.9	8.6

*Notes:*

- (1) Reaction rate parameter of equation (12),  $r_n = 5$  mm.
- (2) Calculations using EFM were made using the same three sets of conditions and body incidence and nose radius, with the reaction rate parameters,  $C_1, \eta_1, C_2, \eta_2$ , given by row II of Table 1.

TABLE 3. Nominal free-stream conditions in test section

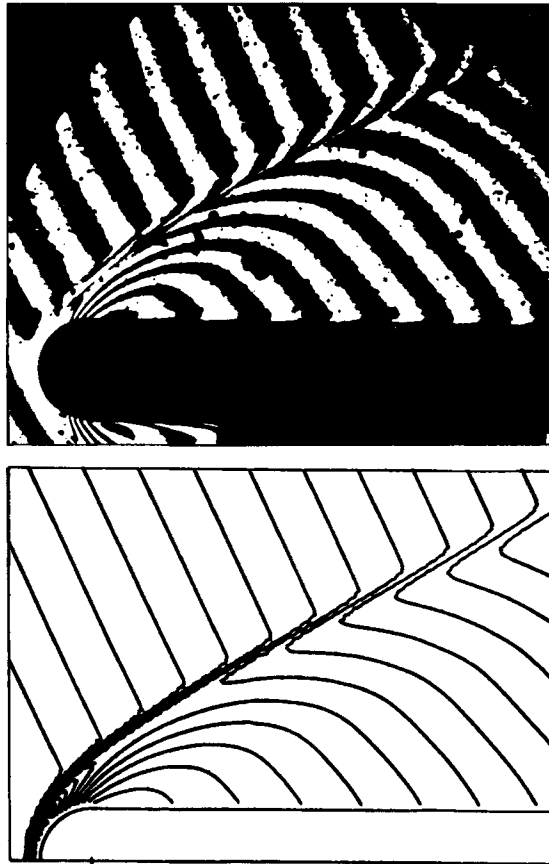


FIGURE 9. Calculated fringe pattern and experimental interferogram taken at  $t = 40 \mu\text{s}$ , with body at zero incidence. Nominal test-section conditions:  $u_\infty = 6.89 \times 10^3$  m/s,  $\rho_\infty = 3.59 \times 10^{-2}$  kg/m<sup>3</sup>,  $T_\infty = 4746$  K,  $\alpha_\infty = 0.149$ ,  $M_\infty = 4.61$ ,  $r_n = 5$  mm,  $\Omega = 12.4$ . ( $C_1, \eta_1, C_2, \eta_2$ ) as for figure 8.

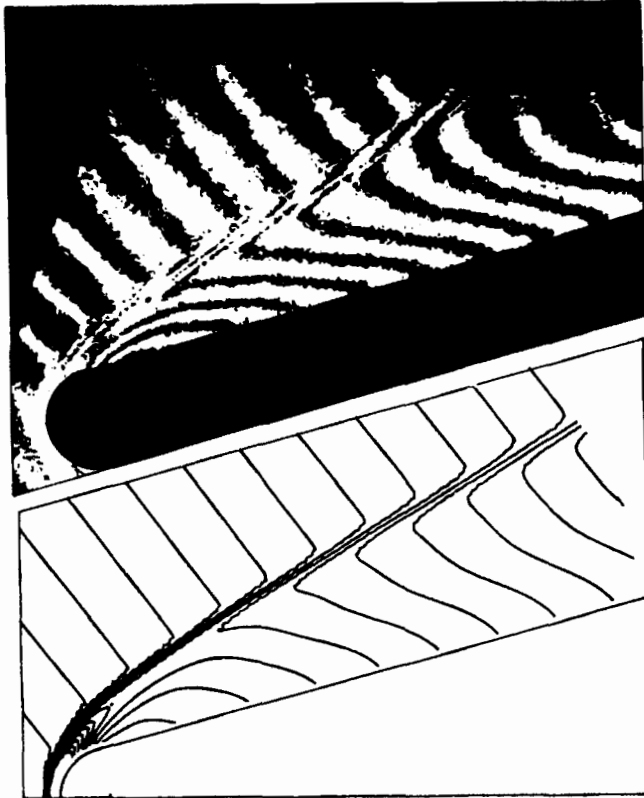


FIGURE 10. Calculated fringe pattern and experimental interferogram taken at  $t = 52 \mu\text{s}$ , with body at  $15^\circ$  incidence. Nominal test-section conditions as for figure 2. ( $C_1, \eta_1, C_2, \eta_2$ ) as for figure 8.  $\Omega = 9.9$ .

estimating the inclination of the shock and assuming the reaction behind the shock is either frozen or infinitely fast. It was found that the fringe shifts for the EFM calculations fell within these limits and it seems safe to assume that the fringe shifts in the experiments would also.

At about halfway along the model the maximum fringe shifts in the experiments and the simulations differed by 0.25, 0.5 and  $-0.2$  fringe widths (or 5%, 12% and 2.5% of the experimental values) for incidences of  $0^\circ$ ,  $15^\circ$  and  $30^\circ$  respectively. At the body surface the difference between experiment and calculations for  $15^\circ$  incidence is about 6%. For  $0^\circ$  incidence the experiments show a small positive fringe shift over most of the afterbody, which implies that the density varies from about 40% above the free-stream density near the nose down to the free-stream density at the rear of the model, whereas the calculations give the density ranging from 35% above the free-stream density to 20% below the free-stream density. These differences are probably within the experimental uncertainties and the limitations of the IDG model. The greatest discrepancy is for  $30^\circ$  incidence (figure 11) for which the experiments show that the fringe shift at the surface is about 30% less than the maximum fringe shift, whereas the simulations show the fringe shift at the surface to be only 2.5% less than the maximum. Although this implies a much higher density at the surface for the calculations than that found in the experiments, this is not compelling evidence of an inadequacy of the calculation. It is more likely that lateral

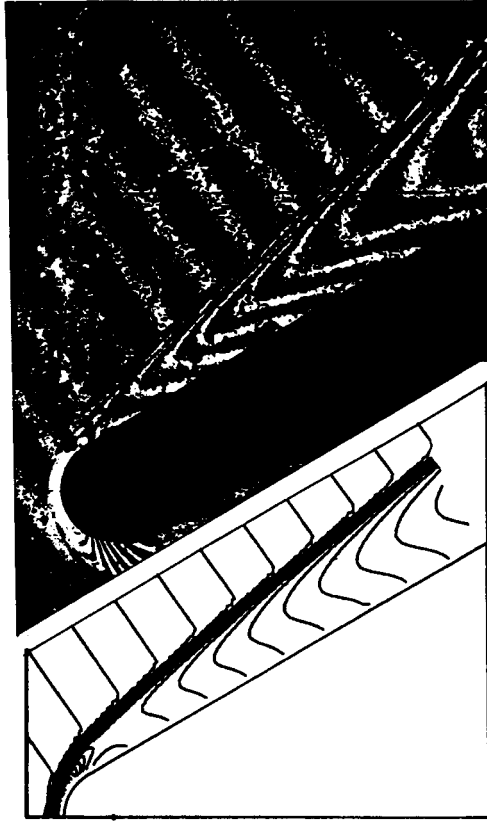


FIGURE 11. Calculated fringe pattern and experimental interferogram taken at  $t = 38 \mu\text{s}$ , with body at  $30^\circ$  incidence. Nominal test-section conditions:  $u_\infty = 6.23 \times 10^3 \text{ m/s}$ ,  $\rho_\infty = 4.31 \times 10^{-2} \text{ kg/m}^3$ ,  $T_\infty = 4256 \text{ K}$ ,  $\alpha_\infty = 0.086$ ,  $M_\infty = 4.56$ ,  $r_n = 5 \text{ mm}$ ,  $\Omega = 8.6$ . ( $C_1, \eta_1, C_2, \eta_2$ ) as for figure 8.

flow spillage, not accounted for in the two-dimensional calculations, is the origin of the low density near the surface shown by the experimental interferogram. Contours of the Mach number for the three different flow fields (figure 12) show that for  $30^\circ$  incidence the Mach number in the afterbody flow is much less than for the other two cases. Since the transverse expansions arising from lateral spillage of flow will propagate across the body at the local Mach angle, they will affect the greatest portion of the afterbody flow for the highest angle of incidence and so the departure from truly two-dimensional flow will be greatest in this case.

## 8. Non-equilibrium effects

Hornung (1976) performed an approximate analysis of the non-equilibrium flow behind a curved shock wave, under the assumption that the flow was far from equilibrium and that therefore the backward (recombination) reaction of (1) could be neglected in comparison with the forward (dissociation) reaction. He concluded that the flow could be conveniently divided into a region of intense reaction close to the shock followed by a large region of chemically frozen flow. This conclusion is supported, in general, by the present EFM calculations even though the recombination rate is not negligible for the density produced in the test section of the

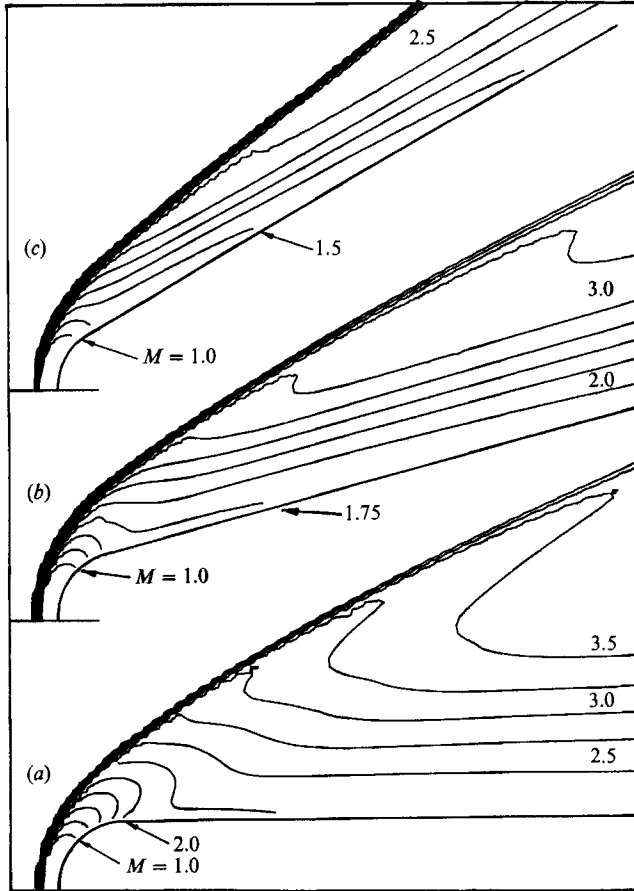


FIGURE 12. Mach-number contours determined from EFM simulations: (a) as for figure 9, (b) as for figure 10, (c) as for figure 11.

shock tunnel. Figure 13 shows the dissociation,  $\alpha$ , along three different streamlines for each of the three angles of incidence of the model. To indicate the departure from equilibrium, an equilibrium dissociation,  $\alpha_e$ , is shown also. This was derived from the local flow state under the assumption that equilibrium is achieved with no change in specific internal energy. The figure shows that the dissociation changes very rapidly near the shock but, in most cases, remains virtually constant (that is, frozen) along the streamline downstream of the shock.

For  $0^\circ$  incidence, the flow is far from equilibrium over most of the flow behind the shock. Along the streamline closest to the body the frozen value of dissociation is greater than the equilibrium value. This chemical freezing, as the flow expands around the nose from a near-equilibrium state adjacent to the stagnation point, is similar to that which occurs in the shock-tunnel nozzle. For the streamlines further from the body, figure 13(a) shows that the dissociation freezes at a value less than the equilibrium value, that is, the reaction rate becomes negligible while the dissociation reaction is dominant. The dissociation rate is given by

$$\left(\frac{d\alpha}{dt}\right)_d = \rho X(\alpha, T) (1 - \alpha) \exp\left(\frac{-\theta_d}{T}\right), \quad (18)$$

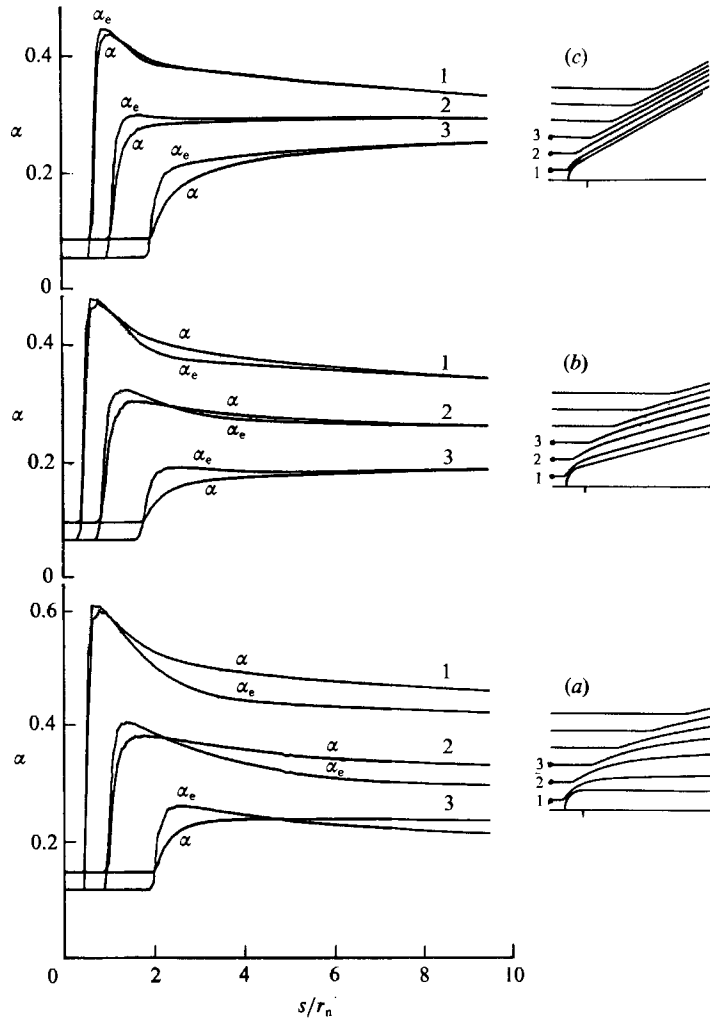


FIGURE 13. Dissociation,  $\alpha$ , and equilibrium dissociation,  $\alpha_e$ , along streamlines, determined by calculation. (a)  $0^\circ$  incidence, (b)  $15^\circ$  incidence, (c)  $30^\circ$  incidence.  $(C_1, \eta_1, C_1, \eta_2)$  as for figure 8.

where  $X(\alpha, T)$  is given by (9), and decreases exponentially as the temperature decreases, while the recombination rate,

$$\left(\frac{d\alpha}{dt}\right)_r = \rho^2 X(\alpha, T) \frac{\alpha^2}{\rho_d}, \tag{19}$$

decreases only as the square of density. Since the mechanism which ‘freezes’ the dissociation is different from that which freezes the recombination, Hornung (1988) and Stalker (1989) have referred to this freezing of the *dissociation* reaction as ‘quenching’.

Figure 14(a) shows the dissociation rate and the recombination rate calculated for conditions along the streamline close to the body and figure 15(a) shows these rates for the streamline further away from the body. The recombination rate is not negligible compared to the dissociation rate but remains virtually constant along the

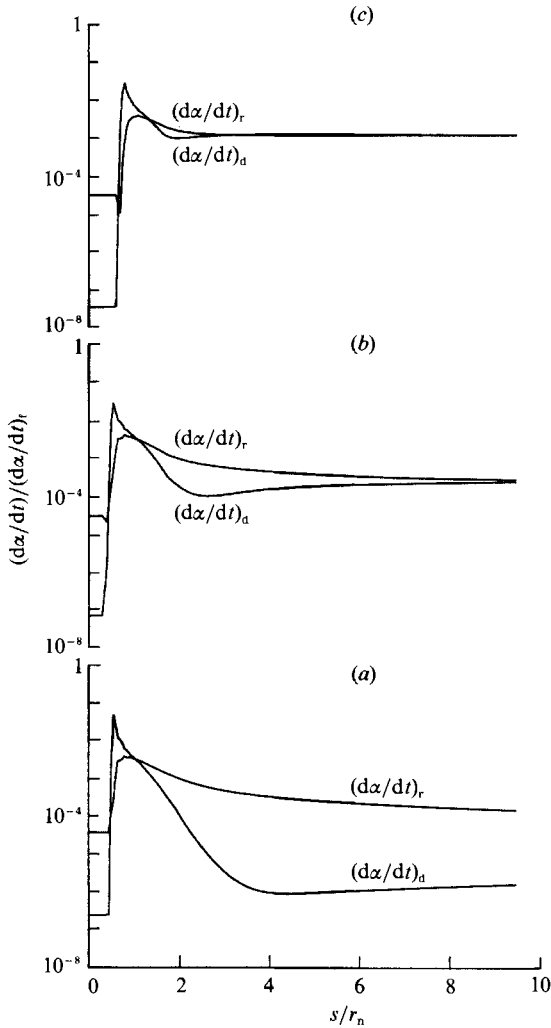


FIGURE 14. Dissociation reaction rate, equation (18), and recombination reaction rate, (19), along streamlines 1 in figure 13. (a)  $0^\circ$  incidence,  $y_\infty/r_n = 0.48$ ; (b)  $15^\circ$  incidence,  $y_\infty/r_n = 0.46$ ; (c)  $30^\circ$  incidence,  $y_\infty/r_n = 0.47$ .  $(d\alpha/dt)_r$  is the reaction rate, (8) and (9), behind a chemical frozen normal shock.  $y_\infty$  is the  $y$ -coordinate of the free-stream streamline.

streamline. Since in both cases  $(d\alpha/dt)_d$  falls by at least an order of magnitude before falling below the value of  $(d\alpha/dt)_r$ , the reaction in both cases may be said to be quenched. Further downstream the very slow recombination reaction becomes dominant and the flow might be described by the conventional term of frozen.

The main difference between the flow along the streamlines shown in figure 13(a) is in the length of the quenched region which precedes the frozen region. Close to the body, the quenched region is negligible and, in any case, could not be resolved adequately using EFM because of the pseudo-dissipative effect of cross-streamline diffusion of the dissociated species, which is most marked near the shock (see Macrossan 1989). Further from the body the quenched region is larger. Stalker (1989) has shown the results of an EFM calculation similar to those here except that the free-stream density was two orders of magnitude less (and the body size was larger).

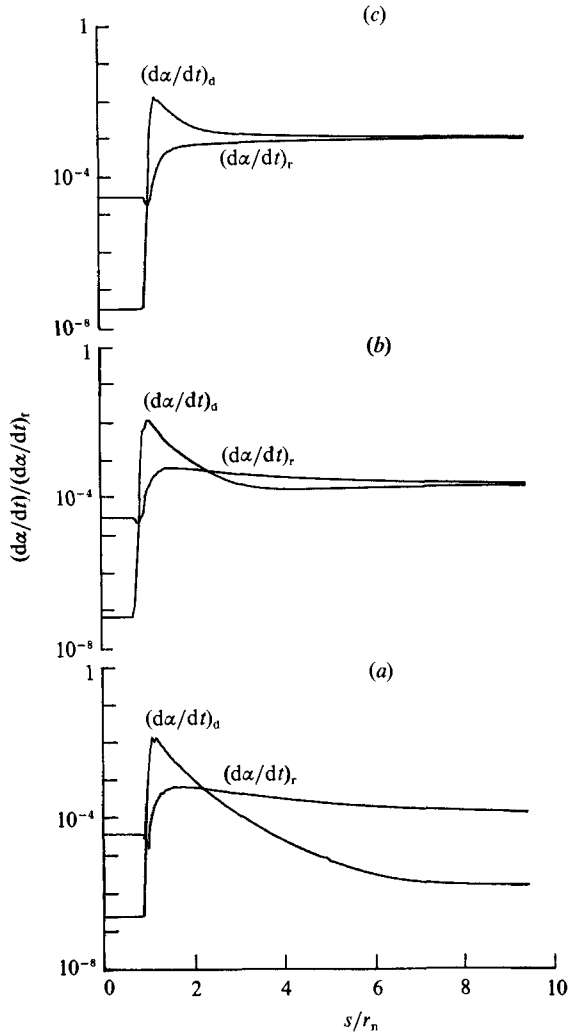


FIGURE 15. Dissociation reaction rate, (18), and recombination reaction rate, (19), along streamlines 2 in figure 13. (a)  $0^\circ$  incidence,  $y_\infty/r_n = 1.42$ ; (b)  $15^\circ$  incidence,  $y_\infty/r_n = 1.34$ ; (c)  $30^\circ$  incidence,  $y_\infty/r_n = 1.35$ . See figure 14.

Such conditions correspond to a highly non-equilibrium regime of the flight trajectory of a re-entry glider at an altitude of about 50 km. In this case the recombination rate was much less than the dissociation rate throughout the flow behind the shock and the quenched region extended over the entire afterbody.

Turning to figures 13(b), 14(b) and 15(b), which show streamline properties for the body at  $15^\circ$  incidence, much the same effects can be seen. Now, however, the frozen region is followed by a region where equilibrium has virtually been reached and, for the streamline furthest from the body, there is no region where the dissociation is frozen above its equilibrium value. Rather there is just a slow dissociation not far from equilibrium. This is also evident when the body is at  $30^\circ$  incidence (see figure 13c, 14c and 15c).

For the three angles of incidence there are distinct non-equilibrium features of the flow over the entire afterbody. An important practical consideration is the effect that

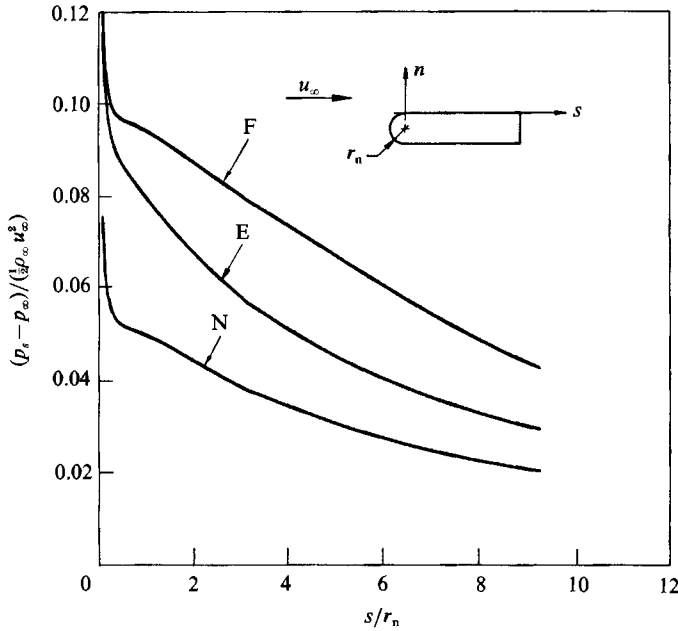


FIGURE 16. Afterbody surface pressures for angle of incidence of  $0^\circ$ . Free-stream conditions corresponding to those in figure 9.: N, non-equilibrium chemistry; E, equilibrium chemistry; F, frozen chemistry.

chemical non-equilibrium may have on the aerodynamic forces on a body immersed in such flows. This is considered in the next section.

## 9. Aerodynamic forces and centre of pressure

For each of the flow fields considered in the experiments EFM has been used to calculate the equilibrium flow and also the flow with the chemical reactions frozen. In the latter case the flow behaves as a perfect gas with a constant ratio of specific heats,  $\gamma$ , which for the IDG model, is given by

$$\gamma = \frac{1}{3}(4 + \alpha_\infty), \quad (20)$$

where  $\alpha_\infty$  is the dissociation in the free stream.

Figures 16, 17, and 18 show the calculated pressures on the afterbody, for three angles of incidence and free-stream conditions corresponding to those in the experiments. Also shown are the pressures calculated for frozen and equilibrium chemistry. In figure 18 there is a noticeable discontinuity in pressure about halfway along the afterbody. This arose from a small error in the specification of the computational grid which resulted in the rear part of the body being at an angle of attack slightly greater than  $30^\circ$ . Figures 17 and 18 also show the Newtonian pressure coefficient and two 'wedge' pressure coefficients, which are derived from the pressure that would act on a sharp wedge having the same inclination as the afterbody, for the two cases of frozen and equilibrium chemistry. Near the rear of the body the pressures are much closer to the wedge pressures than to the Newtonian value for each angle of incidence. An interesting feature of these results is the dip in the pressure profiles at the front of the afterbody in many cases. This may result from

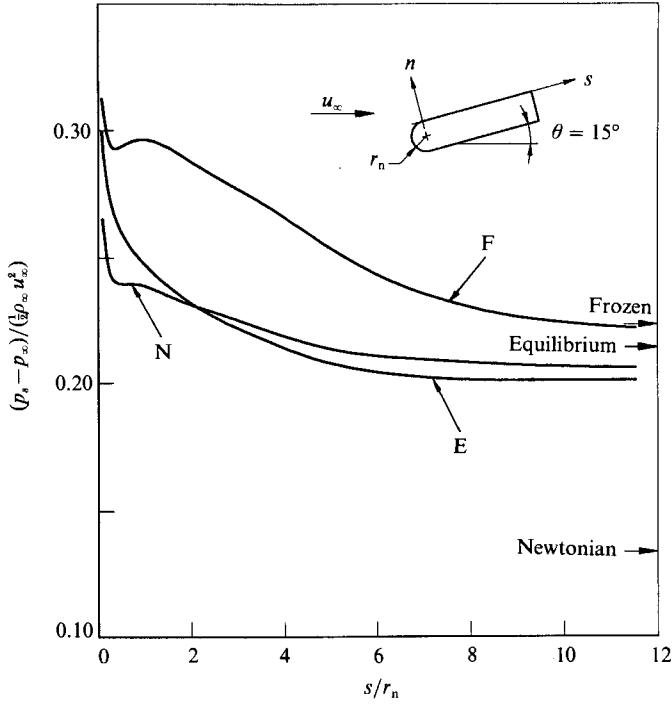


FIGURE 17. Afterbody surface pressures for angle of incidence of 15°. Free-stream conditions corresponding to those in figure 10. See figure 16 for key.

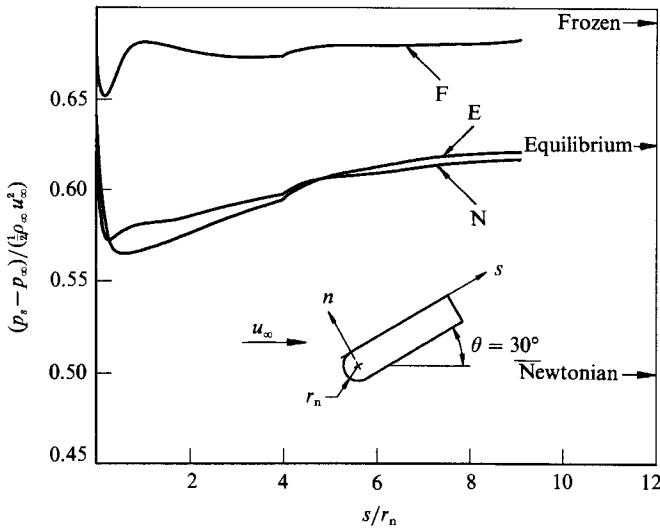


FIGURE 18. Afterbody surface pressures for angle of incidence of 30°. Free-stream conditions corresponding to those in figure 11. See figure 16 for key.

the expansion waves from the blunt nose being reflected back down to the surface from the steep positive gradient of Mach number behind the curved shock.

From the data in figures 16–18 we can determine, for the given free-stream conditions, the pitching moment acting on any body of length  $L$  less than the length

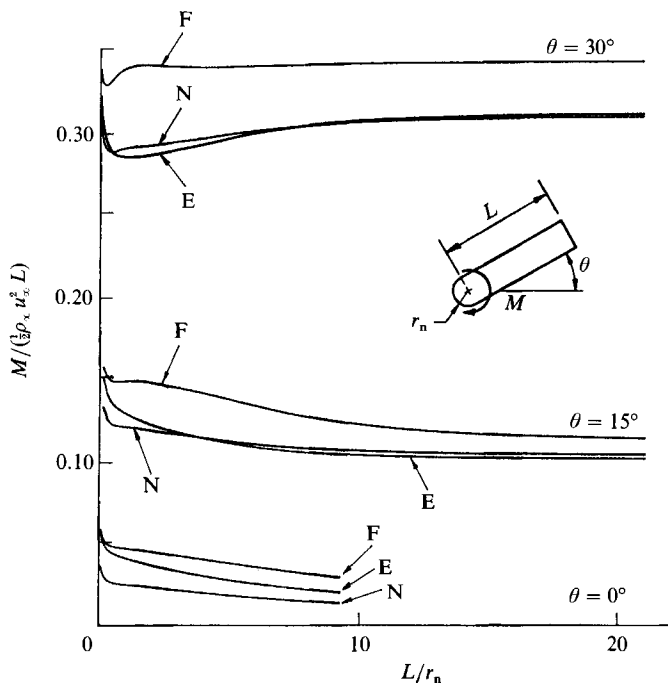


FIGURE 19. Moment coefficients determined from EFM simulations as a function of afterbody length  $L$ , derived from data in figures 16, 17 and 18. Afterbody length in simulations:  $L_{\max}/r_n = 11.7$  for  $\theta = 15^\circ$ ,  $L_{\max}/r_n = 9.5$  for  $\theta = 30^\circ$ . Extrapolations made assuming no change in surface pressure beyond  $L_{\max}$ .

$L_{\max}$  in the computational grid. Furthermore, since for  $15^\circ$  and  $30^\circ$  incidence the pressure comes to a nearly constant value at the rear of the body (figures 17 and 18) the moment for longer bodies may be estimated by assuming that the surface pressure is constant over the extra length of the body. Figure 19 shows the pitching moment coefficients and figure 20 shows the location of the centre of afterbody pressure, each for different lengths of afterbody. Note that, since the pressures acting on the windward side only are taken into account, there is a net pitching moment for  $0^\circ$  incidence.

The important feature of these results is that, while it is possible to get an idea of the magnitude of chemical effects by considering the case of equilibrium chemistry, it is not possible to assume that the results for a chemically reacting gas will lie somewhere between the equilibrium results and those for a perfect gas with frozen chemistry. It is interesting to determine whether this is true for other free-stream conditions, in particular for free-stream conditions typical of hypervelocity flight in the atmosphere. In this case there is no frozen dissociation in the freestream, and for the same stagnation enthalpy, the Mach number is much greater than that produced by the shock tunnel because the atmospheric static temperature is much lower than the static temperature in the shock tunnel.

Simulation calculations were made for typical flight free-stream conditions with the same blunt-nosed body at an angle of attack of  $15^\circ$ . The same free-stream density ( $4.41 \times 10^{-2} \text{ kg/m}^3$ ) as in the experiments was used and this density corresponds to that in the Earth's atmosphere at an altitude of about 25 km. The free-stream temperature was taken as 217 K, which is appropriate for that altitude, and the free-

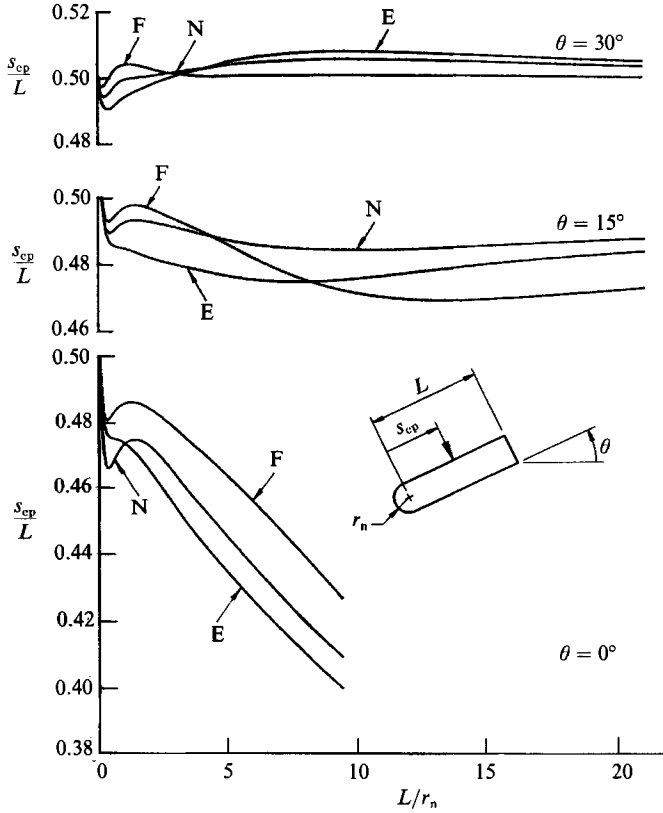


FIGURE 20. Variation of centre of afterbody pressure with  $L$ . As for figure 19.

stream velocity was chosen to give the same stagnation enthalpy ( $H_0 = 28.8$  MJ/kg) as in the experiments. The free-stream Mach number was then 25.8 as opposed to 4.55 in the experiments.

The pressure fields for the shock-tunnel flow and the equivalent flight conditions, each normalized as  $(p - p_\infty) / (\frac{1}{2} \rho_\infty u_\infty^2)$ , are compared in figure 21. The shock is much closer to the body for the higher Mach number, as expected, and the normalized pressure coefficients are about 40% lower. The afterbody force coefficient, given by

$$C_f = (C_x^2 + C_y^2)^{\frac{1}{2}}, \quad (21)$$

where  $C_x$  and  $C_y$  are given by (13) and (14), was  $C_f = 0.29$  for the shock-tunnel flow and  $C_f = 0.18$  for the flight conditions. The corresponding moment coefficients given by (17) were 0.14 and 0.08, which implies a forward shift of the centre of pressure of 3% of the afterbody length for the high-Mach-number flow. Figure 22 shows the surface pressure coefficients calculated for the flight conditions in the three cases of frozen, non-equilibrium and equilibrium chemistry. While these show no strict similarities to the results for the equivalent shock-tunnel flow shown in figure 17 it is clear that the non-equilibrium results are, once again, not intermediate between those for frozen and equilibrium chemistry. Stalker (1989) has argued that some of the unexpected centre of pressure shift experienced by the Shuttle Orbiter on its first re-entry can be explained as the result of chemical non-equilibrium. He presents a number of approximate methods for calculating the effects of chemical non-equilibrium and is able to account for a significant portion of the shift of the centre

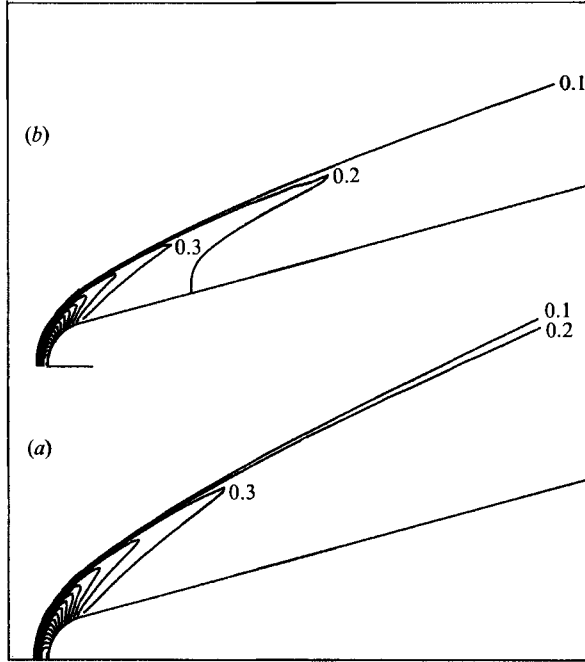


FIGURE 21. Equally spaced contours of  $(p - p_\infty) / (\frac{1}{2} \rho_\infty u_\infty^2) = 0.1, 0.2, 0.3, \dots$  for shock tunnel and 'equivalent' flight free-stream conditions.  $H_0 = 28.8$  MJ/kg,  $r_n = 5$  mm. (a) shock-tunnel flow with free-stream conditions as for figure 2; (b)  $u_\infty = 7.55 \times 10^3$  m/s,  $\rho_\infty = 4.41 \times 10^{-2}$  kg/m<sup>3</sup>,  $T_\infty = 217$  K,  $\alpha_\infty = 0.0$ ,  $M_\infty = 25.8$ ,  $\Omega = 6.8$ . ( $C_1, \eta_1, C_2, \eta_2$ ) as for figure 8.

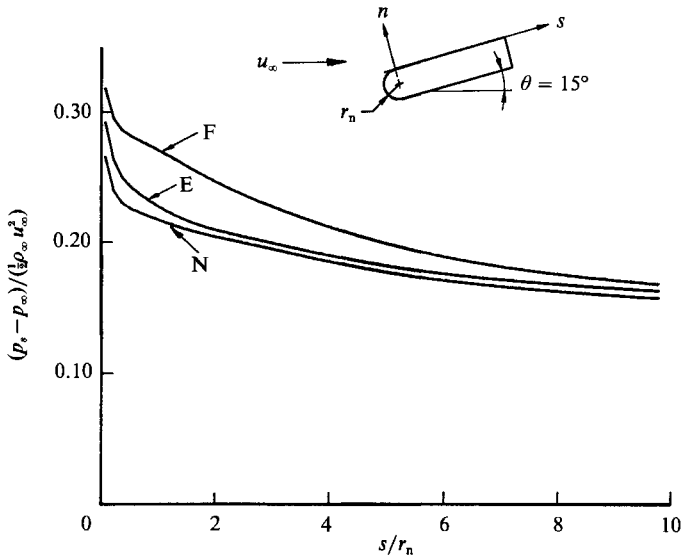


FIGURE 22. Afterbody surface pressure coefficients for flight free-stream conditions corresponding to figure 21 (b): N, non-equilibrium chemistry; E, equilibrium chemistry; F, frozen chemistry.

	Test-section conditions, shock tunnel	Free-stream <sup>(1)</sup> equilibrium conditions	Free-stream <sup>(2)</sup> zero- $\alpha$ conditions
$\rho_\infty$ (kg/m <sup>3</sup> )	$4.31 \times 10^{-2}$	$4.35 \times 10^{-2}$	$3.92 \times 10^{-2}$
$u_\infty$ (m/s)	$6.23 \times 10^3$	$6.17 \times 10^3$	$6.53 \times 10^3$
$T_\infty$ (K)	4256	5472	5182
$\alpha_\infty$	0.086	0.054	0.0
$M_\infty$	4.56	4.06	4.56
$u_\infty^2/2/R_{nn} \theta_d$	0.58	0.57	0.63
$r_n$ (mm)	5.0	4.91	5.76
$\Omega$	8.6	4.7	5.91

Notes:

- (1) These conditions give the same mass, momentum and energy fluxes as in shock tunnel.
- (2) These conditions give the same momentum flux as in the shock tunnel.

TABLE 4. 'Equivalent' wind tunnel flows,  $H_0 = 27.5$  MJ/kg

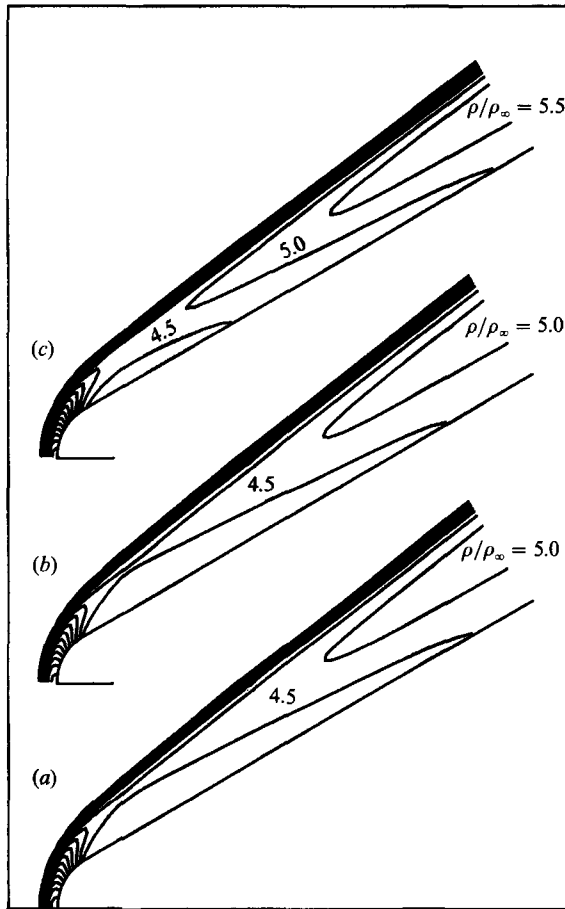


FIGURE 23. Equally spaced density contours,  $\rho/\rho_\infty = 1.5, 2.0, 2.5, \dots$ , for different 'equivalent' free-stream conditions given in table 4 (a) real shock tunnel, (b) equilibrium, (c) zero dissociation. ( $C_1, \eta_1, C_2, \eta_2$ ) as for figure 8.

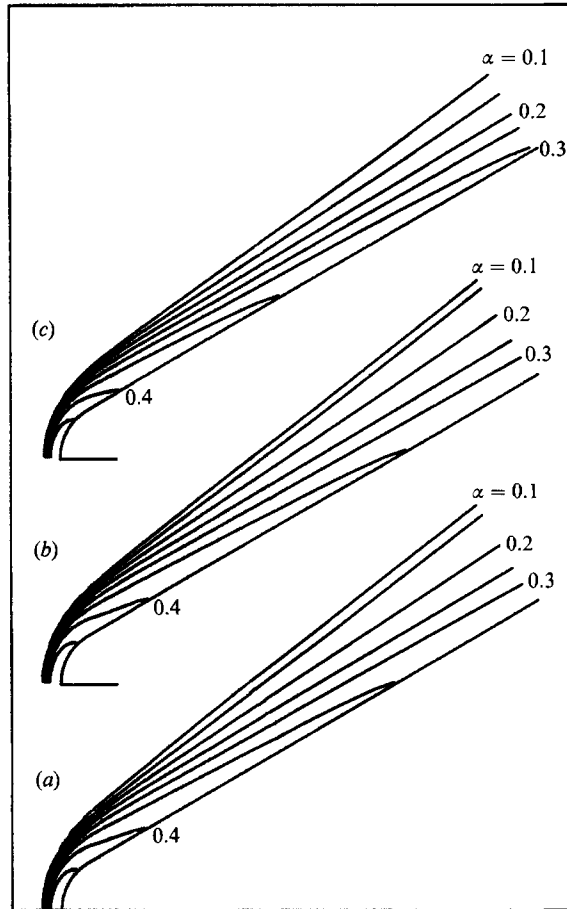


FIGURE 24. Equally spaced dissociation contours,  $\alpha = 0.05, 0.10, 0.15\dots$ , for different 'equivalent' free-stream conditions. See figure 23.

of pressure. What is clear is that, if the centre of pressure on a hypersonic aerodynamic vehicle is crucial to its design, it is desirable that calculations allow for chemical non-equilibrium and that chemical non-equilibrium be produced in any wind tunnel used to test such vehicles.

### 10. Free-stream dissociation effects in wind-tunnel modelling

If the results of wind-tunnel testing are to be used to investigate flows about hypervelocity vehicles, the problems of scaling between shock-tunnel flows and real flight conditions must be addressed. The difference in free-stream Mach number was discussed above and the effects of this were shown in figure 21. A single calculation for the free-stream flight conditions as in figure 21 (b) showed that it was not sufficient to make the hypersonic similarity parameter,  $M_\infty \tau$ , where  $\tau$  is the local body slope, the same for two different bodies in order to obtain flows which are similar (when appropriately scaled), at least when one of the bodies is the blunt body at incidence considered in the experiments reported here. The problem of the Mach-number differences between shock-tunnel test conditions and flight conditions is not considered further here; but the separate problem, that the shock tunnel produces a

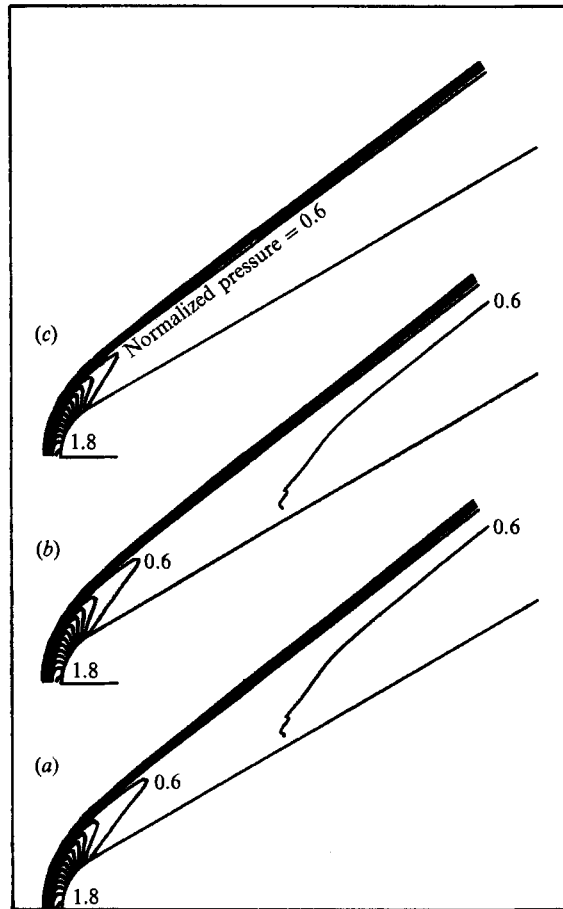


FIGURE 25. Equally spaced pressure contours,  $(p - p_\infty) / (\frac{1}{2} \rho_\infty u_\infty^2) = 0.1, 0.2, 0.3$ , for different free-stream conditions. See figure 23.

degree of frozen dissociation in the free-stream which is not found under flight conditions, is considered in what follows.

Ideally a high-enthalpy wind tunnel, even if it could not produce the required flight Mach number, would at least produce a flow which had no dissociation in the free stream and, furthermore, the free stream would be in local chemical equilibrium. For a given set of typical free-stream conditions in the real shock tunnel it turns out that, for the same stagnation enthalpy, it is not possible to find a set of flow conditions which satisfy the two conflicting requirements (except for the unrealistic case that the free-stream density be increased by many orders of magnitude). However, it is possible to find two different sets of free-stream conditions which are closely related to those in the real shock tunnel and which nearly satisfy the requirements of an 'equivalent' ideal wind tunnel.

The first column of table 4 shows the test-section conditions  $[\rho_\infty, u_\infty, T_\infty, \alpha_\infty]$  which were obtained in the shock tunnel for the run with the flat plate at an angle of attack of  $30^\circ$ . The second column shows the equilibrium conditions  $[\rho_\infty, u_\infty, T_\infty, \alpha_\infty]_e$  which satisfy the condition for chemical equilibrium (equation (2)) and which also give values of the one-dimensional fluxes of mass, momentum and energy which are the

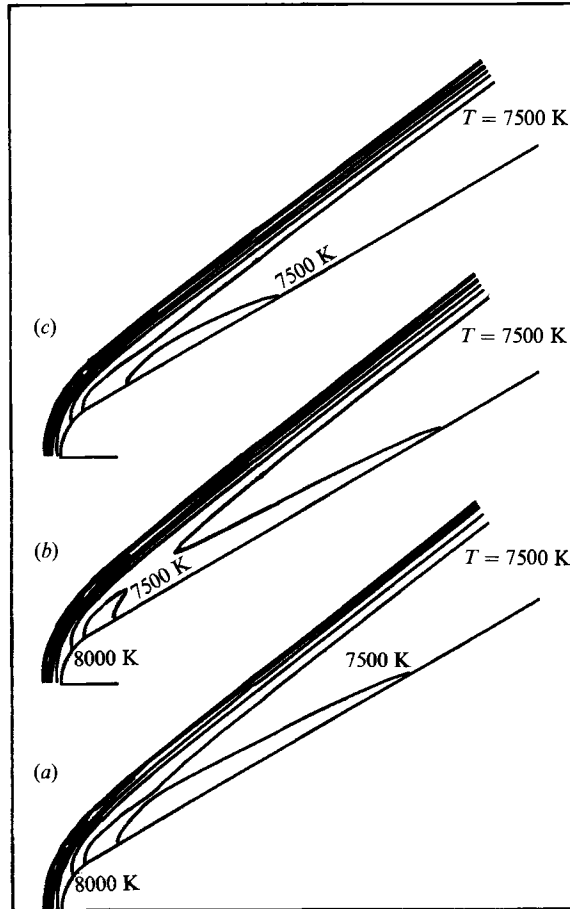


FIGURE 26. Equally spaced temperature contours,  $T = 4500$  K,  $5000$  K,  $5500$  K... for different 'equivalent' free-stream conditions. See figure 23.

same as those produced in the shock tunnel. The flux relations satisfied by these equilibrium conditions are

$$[\rho_\infty u_\infty]_e = \rho_\infty u_\infty, \quad (22)$$

$$[\rho_\infty u_\infty^2 + p_\infty]_e = \rho_\infty u_\infty^2 + p_\infty, \quad (23)$$

$$[\rho_\infty u_\infty \{\frac{1}{2} u_\infty^2 + h_\infty\}]_e = \rho_\infty u_\infty \{\frac{1}{2} u_\infty^2 + h_\infty\}, \quad (24)$$

where the free-stream pressure and specific enthalpy are given by (4) and (5) respectively. To assess the importance of chemical equilibrium in the free stream, calculations were made for the flow about the same body as in the experiments using the free-stream conditions in the second column of table 4. Unfortunately the effects of a small change in Mach number appear also in these calculations.

To eliminate any Mach-number effects and to assess the effects of changing free-stream dissociation, calculations were made with a different set of free-stream conditions  $[\rho_\infty, u_\infty, T_\infty, \alpha_\infty]_0$ , which are shown in the third column of table 4. These conditions give the same stagnation enthalpy and satisfy the constraints (i) that the dissociation be zero ( $\alpha_{\infty,0} = 0.0$ ), (ii) that the Mach number be the same as that in the

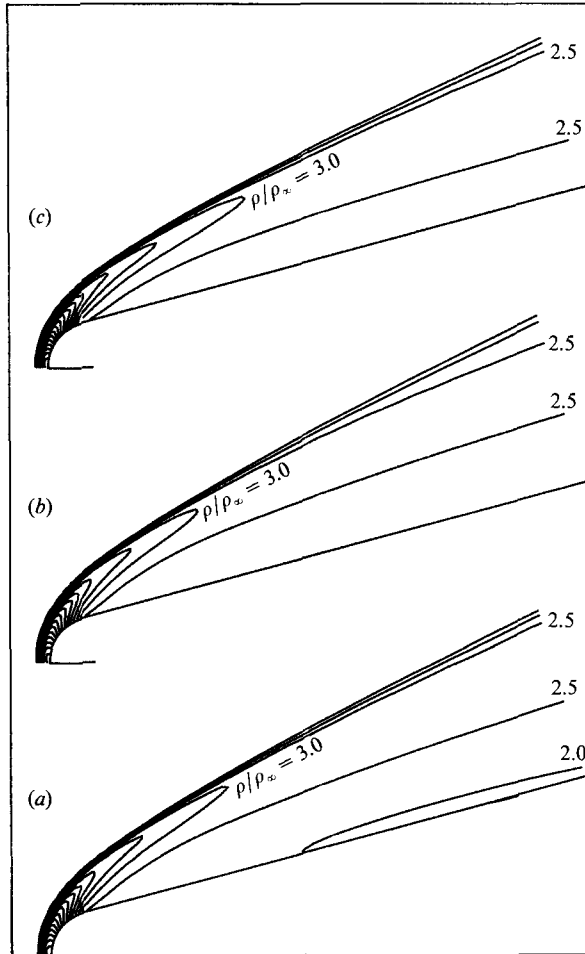


FIGURE 27. Equally spaced density contours,  $\rho/\rho_\infty = 1.5, 2.0, 2.5, \dots$ , for 'equivalent' free-stream conditions. (a) real shock tunnel, figure 2; (b) equilibrium,  $u_\infty = 6.31 \times 10^3$  m/s,  $\rho_\infty = 4.45 \times 10^{-2}$  kg/m<sup>3</sup>,  $T_\infty = 5570$  K,  $\alpha_\infty = 0.064$ ,  $M_\infty = 4.09$ ,  $\Omega = 5.0$ ; (c) zero dissociation,  $u_\infty = 6.67 \times 10^3$  m/s,  $\rho_\infty = 4.00 \times 10^{-2}$  kg/m<sup>3</sup>,  $T_\infty = 5448$  K,  $\alpha_\infty = 0.0$ ,  $M_\infty = 4.55$ ,  $\Omega = 6.0$ . ( $C_1, \eta_1, C_2, \eta_2$ ) as for figure 8.  $H_0 = 28.8$  MJ/kg,  $r_n = 5$  mm.

shock-tunnel test section ( $M_{\infty,0} = M_\infty$ ), and (iii) that the momentum flux is the same as for the real shock tunnel, that is, that

$$[\rho_\infty u_\infty^2 + p_\infty]_0 = \rho_\infty u_\infty^2 + p_\infty.$$

In this case the condition of chemical equilibrium cannot be satisfied. Furthermore, the mass and energy fluxes are each 5% less than these fluxes in the real shock tunnel. It is also possible to replace the constraint (iii) above by the requirement that the mass and energy fluxes be the same as in the real shock tunnel. Such a set of conditions turn out to be very little different from those in the third column of table 4, and EFM calculations showed that the resulting flow was virtually identical to the flow in which the momentum flux was the same as in the shock tunnel.

Calculations with these two new sets of free-stream conditions were made for the body at an incidence of 30° and figures 23, 24, 25 and 26 show the results compared with those calculated for the real shock-tunnel flow. To account for the different

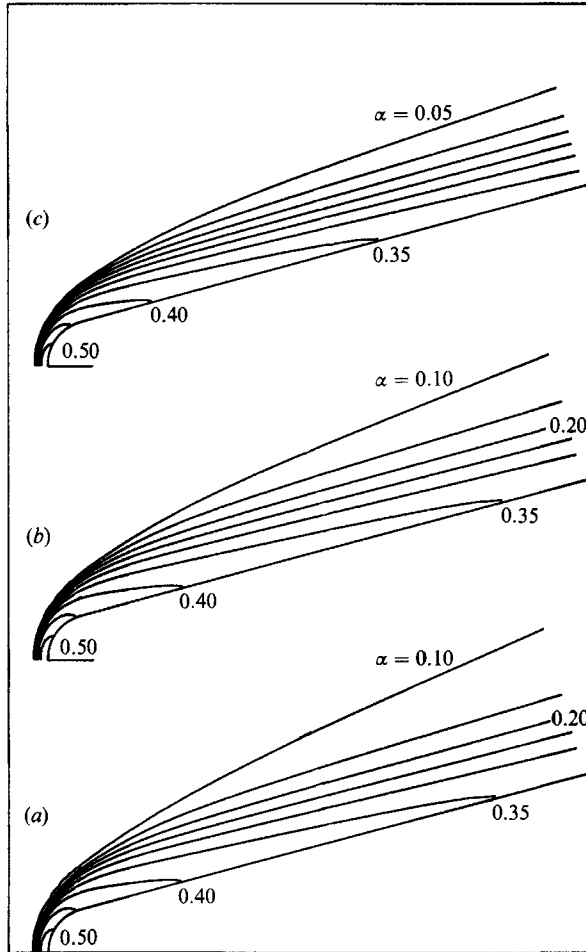


FIGURE 28. Equally spaced dissociation contours,  $\alpha = 0.05, 0.10, 0.15, \dots$ , for 'equivalent' free-stream conditions. See figure 27.

reaction rates expected behind the shock for the different free-stream conditions the body nose radius in the new calculations was selected to make the binary scaling parameter,  $\rho_\infty r_n / u_\infty$ , the same in all calculations. This is a partial compensation only because it is only in flows where the recombination rate is negligible compared with the dissociation rate that the nature of the flow is determined by the binary scaling parameter, and this is not the case in the experiments reported here. In any case the differences in free-stream density were not large.

Figure 23 shows the density contours ( $\rho/\rho_\infty$ ) for the three sets of free-stream conditions. There is very little difference between the real shock-tunnel flow and that calculated for the 'equivalent' equilibrium conditions despite a difference of about 40% in the value of the free-stream dissociation. For zero dissociation in the free stream, however, the density ratio behind the 'afterbody' shock is about 20% greater than in the other two flows and the shock is slightly closer to the body. Figure 24 shows the corresponding values of the degree of dissociation behind the shock and figure 25 shows the pressure fields normalized as  $(p - p_\infty) / (\frac{1}{2} \rho_\infty u_\infty^2)$ . Once again the free-stream equilibrium flow is virtually identical to the real shock-tunnel flow while

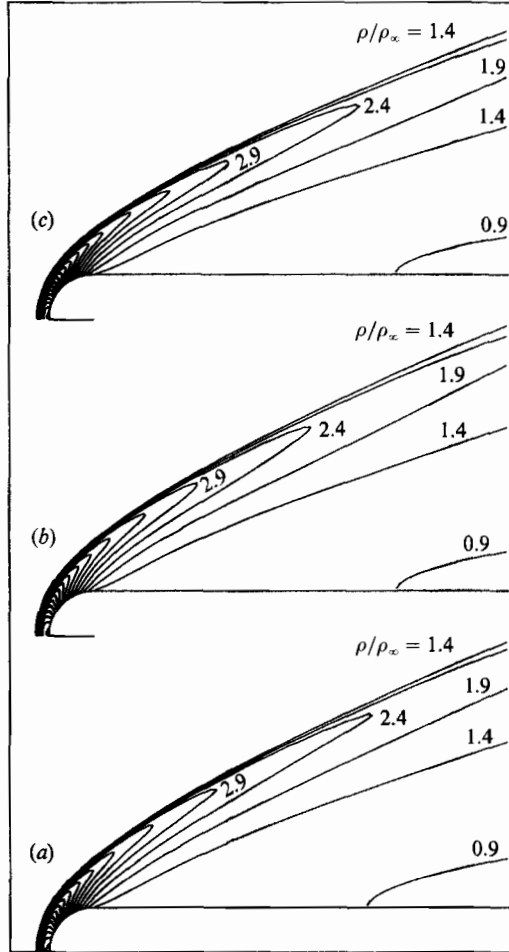


FIGURE 29. Equally spaced density contours,  $\rho/\rho_\infty = 0.9, 1.4, 1.9, \dots$ , for 'equivalent' free-stream conditions: (a) real shock tunnel, figure 9; (b) equilibrium,  $u_\infty = 6.84 \times 10^3$  m/s,  $\rho_\infty = 3.61 \times 10^{-2}$  kg/m<sup>3</sup>,  $T_\infty = 5888$  K,  $\alpha_\infty = 0.119$ ,  $M_\infty = 4.17$ ,  $\Omega = 4.42$ ; (c) zero dissociation,  $u_\infty = 7.34 \times 10^3$  m/s,  $\rho_\infty = 3.15 \times 10^{-2}$  kg/m<sup>3</sup>,  $T_\infty = 6423$  K,  $\alpha_\infty = 0.0$ ,  $M_\infty = 4.61$ ,  $\Omega = 5.3$ . ( $C_1, \eta_1, C_2, \eta_2$ ) as for figure 8.  $H_0 = 34.6$  MJ/kg,  $r_n = 5$  mm.

the zero-dissociation free-stream flow is reasonably close. The afterbody force coefficients given by (21) are 0.67, 0.69 and 0.65 for the real shock tunnel, the equilibrium free-stream and the zero-dissociation free-stream flow and the corresponding pitching moment coefficients, given by (17), are 0.34, 0.35 and 0.33 respectively.

Figure 26 shows contours of temperature behind the shock for the three different free-stream conditions. The absolute temperatures are shown in order to demonstrate some similarities in the flows since it was found that contours of  $T/T_\infty$  were quite different in the three cases. Because of the large value of dissociation temperature ( $\theta_d = 113200$  K) the temperature field is affected greatly by small changes in the degree of dissociation, and the temperature fields in figure 26 probably differ enough to change significantly the heat transfer rates to the body surface in any experiment in wind tunnels having these different free-stream conditions.

Similar calculations, with equilibrium and zero dissociation in the free stream,

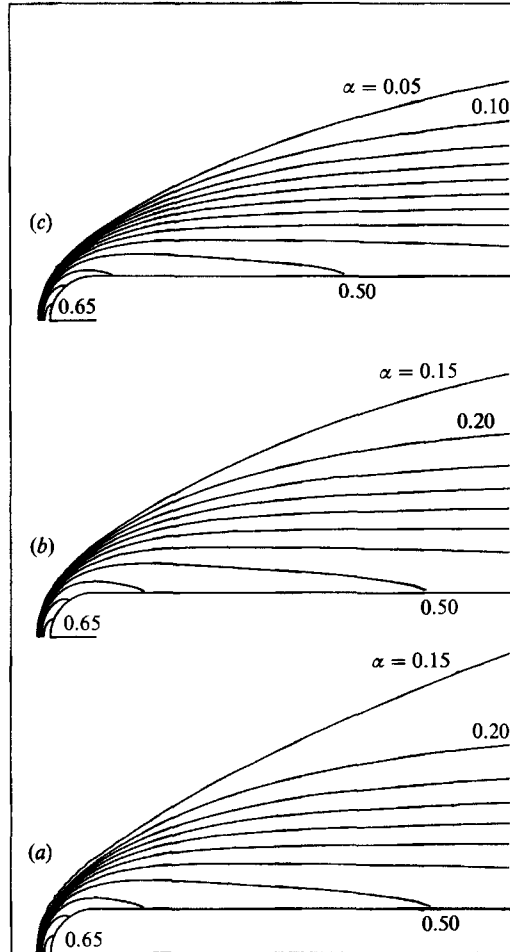


FIGURE 30. Equally spaced dissociation contours,  $\alpha = 0.05, 0.10, 0.15, \dots$ , for 'equivalent' free-stream conditions. See figure 29.

were made with the body at angles of incidence of  $15^\circ$  and  $0^\circ$ . Figure 27 shows the density contours and figure 28 the dissociation contours for  $15^\circ$  incidence, and figures 29 and 30 show these for  $0^\circ$  incidence. For both angles of incidence the density contours are much the same for each of the three sets of free-stream conditions, despite the differences in the degree of dissociation near the shock. The dissociation levels near the body are similar for the different free-stream conditions. The afterbody force coefficients for  $15^\circ$  incidence are  $C_f = 0.29, 0.30$  and  $0.27$  for the real shock-tunnel flow, the equilibrium free stream and the zero-dissociation free stream respectively. The corresponding values for  $0^\circ$  incidence are  $C_f = 0.10, 0.11$  and  $0.09$ .

These calculations have shown that, for the three angles of incidence, it makes little difference whether or not the free stream is in equilibrium, at least when the departure from equilibrium dissociation is of the order of  $\Delta\alpha_\infty \approx 0.03$ , as it is in the shock-tunnel test section. Larger changes in  $\alpha_\infty$ , of the order of the difference between  $\alpha_\infty = 0$  found in flight conditions and the values of  $\alpha_\infty \approx 0.1$  produced by the shock tunnel, have some effect on the flow behind the shock wave, but the general nature of the flow is unaffected. This is despite the fact

that the two flows differ not only in the degree of frozen free-stream dissociation, but also in the direction in which the reactions, equation (1), are running in the free stream. That is, the free-stream gas mixture is recombining very slowly in the real shock tunnel, whereas in the equivalent flow having zero dissociation in the free stream the mixture is dissociating.

## 11. Conclusions

The flows considered here were for the important case of dissociating flow over a straight blunt-nosed body. A curved shock wave is established ahead of the blunt nose and the gas which passes through the shock is dissociated and subsequently expands, by varying amounts on different streamlines, around the curved nose before flowing over the afterbody. The effects of this dissociation and rapid expansion, in which chemical equilibrium cannot be maintained, can extend for a large distance downstream of the blunt nose. The calculations have shown that some idea of the magnitude of real gas effects on the aerodynamic pressures acting on a body can be obtained by assuming that chemical composition throughout the flow is in local equilibrium. However, such equilibrium calculations can give misleading predictions of the location of the centre of pressure. Furthermore, it has been shown that the pressure forces acting on a body when the flow is not in chemical equilibrium are not always intermediate between those for frozen and equilibrium chemistry. An important feature of the flow, first investigated by Hornung (1976), is the rapid quenching of the dissociation reaction. To understand such flows a proper consideration of chemical non-equilibrium is required, in both computational and experimental investigations.

The calculations have shown that a strongly dissociating flow can be produced by the free-piston driven shock-tube wind tunnel. This shock tunnel produces test flow velocities which are typical of the flight of proposed hypervelocity aerospace planes. Although the test time in the shock tunnel is extremely short the calculations have shown that it is long enough to obtain a fully developed flow over a typical model. The results from the shock tunnel have been used here to validate the computational method and the important question of whether such test flows can yield information which would be useful for detailed aerodynamic design of aerospace planes has been dealt with only briefly. This is a difficult question and a first step towards its answer has been made by considering the flow in two hypothetical 'equivalent' wind tunnels which are supposed to produce flows of the same stagnation enthalpy as in the real shock tunnel but do not produce all those conditions of the real shock-tunnel flow which are different from those found in flight in the atmosphere. In this way, it has been shown that the frozen degree of dissociation in the test section of the shock tunnel appears to be not very important, at least as far as the aerodynamic forces acting on the model are concerned; a wind tunnel producing equilibrium dissociation in the test section at much the same temperature and density would produce results virtually identical to those in the real shock tunnel, and a wind tunnel with zero dissociation in the free-stream at the same Mach number would produce results reasonably similar.

More important is the difference between the flows at high supersonic free-stream Mach number ( $M_\infty \approx 5$ ) which are produced in the shock tunnel and flows at hypersonic Mach number ( $M_\infty \approx 25$ ) which are typical of the flight of aerospace planes. For the flow about a blunt-nosed body considered here the hypersonic similarity law for slender-body flows, that is  $M_\infty \tau = \text{constant}$ , was not sufficient to

find an equivalent flow for typical flight conditions. Although the problem of Mach number effects was only touched upon in this work, the conclusions of the previous paragraph indicate that there is good reason to hope that these effects can be decoupled from the question of chemical non-equilibrium in the free stream.

I thank R. J. Stalker for making his experimental results available to me. These results were obtained at the Australian National University using the T3 facility which was operated there by Mr V. Adams. The computational part of this work was supported by the Australian Research Council, Grant A48715757.

#### REFERENCES

- APPLETON, J. P., STEINBERG, M. & LIQUORNIK, D. J. 1968 Shock-tube study of nitrogen dissociation using vacuum-ultraviolet light absorption. *J. Chem. Phys.* **48**, 599.
- BAULCH, D. L., DRYSDALE, D. D., HORNE, D. G. & LLOYD, A. C. 1973 *Evaluated Kinetic Data for High Temperature Reactions*. Butterworths.
- BIRD, G. A. 1976 *Molecular Gas Dynamics*. Clarendon.
- BYRON, S. 1966 Shock-tube measurement of the rate of dissociation of nitrogen. *J. Chem. Phys.* **44**, 1378.
- CARY, B. 1965 Shock tube study of the thermal dissociation of nitrogen. *Phys. Fluids* **8**, 26.
- CRANE, K. C. A. & STALKER, R. J. 1977 Mass-spectrometric analysis of hypersonic flows. *J. Phys. D: Appl. Phys.* **10**, 679.
- FREEMAN, N. C. 1958 Non-equilibrium flow of an ideal dissociating gas. *J. Fluid Mech.* **3**, 407.
- GRIFFITH, B. J., MAUS, J. K., MAJORS, B. M. & BEST, J. T. 1987 Addressing the hypersonic simulation problem. *J. Spacecraft* **24**, 334.
- HANSON, R. K. & BAGANOFF, D. 1972 Shock-tube study of nitrogen dissociation rates using pressure measurements. *AIAA J.* **10**, 211.
- HORNUNG, H. G. 1972 Non-equilibrium dissociating nitrogen flow over spheres and circular cylinders. *J. Fluid Mech.* **53**, 149.
- HORNUNG, H. G. 1976 Non-equilibrium ideal dissociation after a curved shock wave. *J. Fluid Mech.* **74**, 143.
- HORNUNG, H. G. 1988 Experimental real-gas hypersonics. *Aero. J.* **92**, 379.
- KEWLEY, D. J. & HORNUNG, H. G. 1974 Free-piston shock-tube study of nitrogen dissociation. *Chem. Phys. Lett.* **25**, 531.
- LIGHTHILL, M. J. 1957 Dynamics of a dissociating gas. Part 1. Equilibrium flow. *J. Fluid Mech.* **2**, 1.
- MACROSSAN, M. N. 1989 The equilibrium flux method for the calculation of flows with non-equilibrium chemical reactions. *J. Comput. Phys.* **80**, 204.
- MACROSSAN, M. N. & STALKER, R. J. 1987 After-body flow of a dissociating gas down stream of a blunt nose. *AIAA Paper* 87-407.
- MARRONE, P. V. 1962 Normal shock waves in air. *CAL Rep. AG-1729-A-2*.
- MAUS, J. R., GRIFFITH, B. J. & SZEMA, K. Y. 1984 Hypersonic Mach number and real gas effects on Space Shuttle Orbiter aerodynamics. *J. Spacecraft* **21**, 136.
- MUDFORD, N. R. & STALKER, R. J. 1976 The production of pulsed nozzle flows in a shock tube. *AIAA Paper* 76-357, (*AIAA 9th Fluid and Plasma Dynamics Conference, San Diego, Calif.*).
- MUDFORD, N. R. & STALKER, R. J. 1980 Hypersonic nozzles for high enthalpy non-equilibrium flow. *Aero. Q.* **31**, 113.
- PULLIN, D. I. 1980 Direct simulation methods for compressible inviscid ideal gas flow. *J. Comput. Phys.* **34**, 231.
- STALKER, R. J. 1989 Approximations for non-equilibrium hypervelocity aerodynamics. *AIAA J.* (to appear).
- VINCENTI, W. G. & KRUGER, C. H. 1965 *An Introduction to Physical Gas Dynamics*. Wiley.